This is a manuscript preprint submitted to EarthArXiv. This paper is under review in Sedimentology. The authors welcome feedback on this article.

Quantitative palaeohydrology reveals fluvial response to early-mid Triassic climate change

Xiang Yan, Alexander C. Whittaker and Gary J. Hampson*

Department of Earth Science and Engineering, Imperial College London, London SW7 2AZ, UK

***Correspondence:** Xiang.yan19@imperial.ac.uk

Abstract

Anthropogenic climate change represents the greatest modern forcing on global river dynamics. Investigating the sensitivity of rivers to past climate in the geological record is thus crucial in understanding future landscapes in a warming world. The Sherwood Sandstone Group, UK, a unit of early-middle Triassic (c. 248-239 Ma) dryland fluvial deposits, records the protracted climatic-biotic recovery period following the Permo-Triassic Mass Extinction. We quantify the evolution of this fluvial system, exposed in the southwest UK, by combining facies-scale sedimentology with a numerical palaeohydraulic workflow. We reconstruct key hydraulic and geomorphic characteristics, showing that gravel-bed lower Triassic rivers had palaeoslopes between 1.0×10^{-3} and 2.0×10^{-3} m/m and bankfull water discharges of c. 600 m^3/s. During the middle Triassic, rivers were sand-bedded, with palaeoslopes between 8×10^{-2} and 5×10^{-2} m/m. Bankfull water discharges ranged between 290 and 360 m^3/s: half those

of the lower Triassic. This halving of bankfull discharge occurs despite an inferred eightfold increase in catchment area in the mid-Triassic and stable levels of long-term precipitation, and is attributed to lower Triassic catchments generating highly intermittent, disproportionately large bankfull flow events. Coupled with the very coarse grain size recorded in the Lower Triassic and regional stratigraphic correlations to similar conglomerate sheets across NW Europe, we attribute this to a global hyperthermal event: the Late Smithian Thermal Maximum (c. 248 Ma). Rapid warming during a greenhouse interval triggered widespread landscape devegetation, bedrock erosion, and extreme, infrequent monsoonal precipitation. Our results demonstrate the ability of quantitative palaeohydrology to produce numerically-informed depositional models, and to identify the impacts of extreme global warming.

1. Introduction

Fluvial stratigraphy provides a valuable archive of landscape response to environmental and tectonic forcings in the geological past (Romans et al., 2016; Castelltort et al., 2023; McLeod et al., 2025). Rivers are highly sensitive to climate change through their discharge regime (e.g. Larkin et al., 2020; Satoh et al., 2022; McLeod et al., 2024, Wang et al., 2024), so understanding how ancient fluvial systems responded to and recorded these drivers is of key importance for constraining the impact of future climate change, given that 1.5-4.5°C of anthropogenic global warming is forecasted by 2100 (Meinshausen et al., 2011; Van Vuuren et al., 2026). Globally, drylands are the largest continental ecosystem by area, covering 40% of the Earth's land surface, and support a third of the global population (Millennium Ecosystem Assessment, 2005; Safriel et al., 2005) so constraining the behaviour of dryland rivers in the geological record is particularly crucial for addressing landscape sensitivity to climate.

Internationally, the deposits of dryland fluvial systems also serve as important reservoir units for geothermal energy and the geological storage of carbon dioxide, both key

components of the energy transition (e.g. Schellschmidt et al., 2010; Mijnlieff, 2020; Hjelm et al., 2020; English et al., 2024; Gasanzade and Bauer, 2025). A better understanding of their dynamics would also allow us to refine depositional models for these reservoirs (e.g. Lang et al., 2004; Menacherry et al., 2009; McKie, 2011; Morón et al., 2014; Newell and Shariatipour, 2016; Henares et al., 2020; Hossain et al., 2024).

Facies-based sedimentological analysis can be an effective tool to understand the dynamics of past fluvial systems (e.g. Blum and Törnqvist, 2000; Miall, 2006; Colombera et al., 2013; Plink-Björklund et al., 2015; Fielding et al., 2018). However, dryland fluvial deposits are often biotically sparse or barren, limiting the availability of climate proxy data which is crucial in inferring external forcings. A complementary approach is the use of palaeohydraulic methods, which employ direct measurements of the preserved stratigraphic record, such as grain size and the thickness and distribution of cross-strata to reconstruct fluvial behaviour, and have increasingly offered the potential to quantify river dynamics in the geological past (e.g. Leclair and Bridge, 2001; Trampush et al., 2014; Bradley and Venditti, 2017; Long et al., 2021). In principle, these methods enable us to go further than insights from facies-based analyses alone, particularly when such approaches are combined carefully with descriptive and qualitative facies observations from stratigraphy (e.g. Bhattacharya et al., 2016; Lyster et al., 2021; Wood et al., 2022; 2025; Sharma et al., 2023; McLeod et al., 2023; 2025; Valenza et al., 2026).

This study exemplifies this approach for the Sherwood Sandstone Group (SSG) of the British Isles, a regionally significant unit of Triassic fluvial and aeolian sandstones, deposited in central Pangaea at low latitudes in a dryland setting (**fig. 1a, b)** (c. 250 to 239.6 Ma, Yan et al., 2026). The SSG holds particular climatic significance, as it records the prolonged recovery period following the Permo-Triassic Mass Extinction (e.g. Bourquin et al., 2011; Radley and Coram, 2016; Newell, 2017b). Depositional models for the SSG are also of interest, as the unit is a significant reservoir unit for geothermal energy (Downing et al., 1984; Moscardini et al., 2025; Brémaud et al., 2026), the geological storage of carbon dioxide (e.g. Chedburn et

al., 2022; English et al., 2024; Hossain et al., 2024; Breeze et al., 2026) and groundwater resources in the UK (e.g. Plant et al., 1999; Newell and Smith, 2009; Medici et al., 2019). The SSG hence serves both as a unit of significance for the energy transition, as well as preserving a record of the aftermath of the most extreme climatic-biotic turnover of the Phanerozoic (Benton and Newell, 2014; Radley and Coram, 2016; Newell, 2017a; b).

A complete section of the SSG crops out on the south coast of Devon in the southwest UK, at the western edge of the Wessex Basin (**fig. 1b, c**). Owing to the continuity and quality of outcrop, the SSG here has a long history of characterisation (e.g. Smith, 1990; Smith and Edwards, 1991; Hounslow and McIntosh, 2004; Morton et al., 2013; Hounslow et al., 2017; Newell, 2017b; Hounslow and Gallois, 2023). Thus, the Devon coastal section represents an ideal location to apply quantitative palaeohydraulic methods to quantify the changing fluvial character of a dryland system through the lower to middle Triassic.

Here, we reconstruct the palaeohydraulic character of the rivers of the SSG for the first time using a quantitative palaeohydrological framework. Combined with the results of facies-based sedimentology, we derive parameters such as river palaeoslope, planform, bankfull water discharge and bankfull sediment flux to produce updated, quantitatively informed depositional models, referenced against modern rivers. In addition, we evaluate the external forcings behind the changing character of fluvial deposition in the SSG, especially in relation to the recovery period following the Permo-Triassic Mass Extinction.

2. Geological and palaeoclimatic setting

The SSG was deposited in a series of linked, extensional basins formed during the initial phase of supercontinent breakup (e.g. Bourquin et al., 2011; McKie, 2017). The SSG overlies the existing Permian basin fill, and underlies the Mercia Mudstone Group, a unit of playa and lacustrine mudstones (e.g. Howard et al., 2008; Newell, 2024). The SSG is composed of the Chester Formation (CHF), the Wilmslow Sandstone Formation and the

Helsby Sandstone Formation (HSF) (Ambrose et al., 2014). The CHF and HSF were deposited by two, long-distance, north-flowing river systems (**fig. 1b,** e.g. Tyrrell et al., 2012; Morton et al., 2013; 2016; Franklin et al., 2020) with distinct source areas and sedimentological character (Morton et al., 2016, Yan et al., 2026). On the source-to-sink scale, the rivers of the CHF have been designated as the 'Sherwood 1 River System', and the rivers of the HSF designated as the 'Sherwood-2 River System' (Yan et al., 2026).

In Devon, the CHF is approximately 30 m thick and conglomeratic (Smith, 1990; Smith and Edwards, 1991). The HSF is approximately 200 m thick and is dominated by sandstone (Newell, 2017b). The CHF and HSF are separated by a palaeosol horizon and an aeolian deflation surface (e.g. Leonard et al., 1982; Wright et al., 1991; Hart, 2014) which represents the Mid-Triassic Unconformity (*sensu* Newell, 2017b), and the Wilmslow Sandstone Formation is absent. In older, local lithostratigraphic nomenclature, the CHF is known as the Budleigh Salterton Pebble Beds, and the HSF as the Otter Sandstone (Ambrose et al., 2014). In Devon, the change in sediment routing between the Sherwood-1 (CHF) and Sherwood-2 river systems (HSF) manifests as a substantial expansion in catchment area for the rivers of the HSF compared to those of the CHF, inferred from quantitative provenance analysis (**fig. 1b**, Morton et al., 2013). This regional drainage reorganisation was likely driven by the Hardegsen tectonic event (Bourquin et al., 2011; von Eynatten et al., 2026).

Though not formally divided into lithostratigraphic members, the CHF can be divided into two architecturally distinct units, representing river deposits of differing fluvial character (**fig. 2;** Smith, 1990; Smith and Edwards, 1991). The HSF has a well-defined lithostratigraphy, and is divided into four members. Each member is bounded by major erosion surfaces, and possesses distinct sedimentological, geochemical and heavy mineral characteristics (Morton et al., 2013; Newell, 2017b). The lowermost unit of the HSF is the 15 m thick aeolian West Down Member (**fig. 2**), which is restricted to the Devon coastal section (Smith and Edwards, 1991; Newell, 2017b). The overlying succession is dominantly fluvial, and comprises the Otterton Ledge, Chiselbury Bay and Pennington Point members, which are c. 115 m, 50 m

and 20 m thick, respectively (Newell, 2017b). Previous interpretations of fluvial planform have been made from sedimentary architectural analysis, suggesting that the majority of the SSG was deposited by braided rivers in accordance with the multistorey, multilateral channel-fill sandstone complexes which dominate the unit (e.g. Sellwood et al., 1984; Purvis and Wright, 1991; Newell, 2017b; Coram et al., 2019).

The age of the CHF is constrained to the Olenekian Stage of the lower Triassic by magnetostratigraphy (**fig. 2,** Hounslow et al., 2017). Regional correlation to Triassic deposits in the Permian Basin (**fig. 1a**), which are dated using biostratigraphy and magnetostratigraphy (Bachmann and Kozur, 2004; Durand, 2006; Sass et al., 2023), further suggest a probable Smithian age for the CHF (c. 250 – 248 Ma; Durand, 2006; Bourquin et al., 2011). During this time, continued activity from the Siberian Traps Large Igneous Province resulted in prolonged global climatic instability after the onset of the Permo-Triassic Extinction at 251.9 Ma (Ogg et al., 2020). This resulted in a fluctuating but consistently hothouse climate, as reflected in the global $\delta^{13}C$ isotope record (**fig. 2,** Benton and Newell, 2014; Sun et al., 2026). Fossils are particularly scarce in the CHF (Ambrose et al., 2014; Dunhill et al., 2013). The age constraints for the CHF overlap with the Late Smithian Thermal Maximum (LSTM), the final and most extreme hyperthermal of the lower Triassic, which was triggered by the Siberian Large Igneous Province (Du et al., 2022). During the LSTM, continental temperatures peaked at 35-40°C, resulting in significant perturbations to the global biosphere (Sun et al., 2012; Linström et al., 2019). Although climate in general has been suggested as a driver for the deposition of the CHF (Radley and Coram, 2016; Newell, 2017a), alternate forcings, such as tectonic activity (Wills, 1956; Gallois, 2014) and more proximal sediment sourcing (Wills, 1970; Burgess et al., 2025) have also been proposed to account for the coarse grain size of this unit.

The chronology of the mid-Triassic HSF is well-constrained using magnetostratigraphy and the radiometric dating of rhizocretonary calcite (**fig. 2**, Purvis et al., 2025; Yan et al., 2026). The West Down and Otterton Ledge members have a combined duration of 5.3 Ma (246.5-241.2 Ma), the Chiselbury Bay Member spans 1.0 Myr (241.2-240.2 Ma), and the Pennington Point Member represents 0.6 Myr (240.2-239.6 Ma) (**fig. 2**). By this time, the cessation of the

Siberian Traps Large Igneous Province allowed the climate to stabilise and the biosphere to recover (**fig. 2,** Newell, 2017a). In contrast to the biotically barren CHF, the HSF is characterised by an abundance of fossil vegetation, and a diverse assemblage of vertebrate fossils, including fish, amphibians and reptiles (Benton and Spencer, 1995; Newell, 2017b; Coram et al., 2019).

The boundary between the HSF and the mid- to late-Triassic Mercia Mudstone Group is strongly diachronous across the British Isles (e.g. Hounslow and Gallois, 2023; Yan et al., 2026). This diachroneity represents a north-to-south transgression of Mercia Mudstone Group playa lake facies and a resultant shortening of the Sherwood-2 River System, and coincides with a regional aridification and the Muschelkalk transgression in the Tethys Ocean (Bourquin et al., 2011; McKie, 2017; Newell, 2017a).

3. Methods

3.1. Overview of primary data collection and workflow

Our data collection and workflow is summarised in **fig. 3**, with data and extended methods in **Supplementary Material 1, 2**. Primary field data for palaeohydrological analysis include dune-scale measurements of cross bedding, barform-scale architectural measurements, bar accretion direction and dune-scale palaeocurrents (**e.g. figs. 4, 5**), and measurements of sediment grain size (**e.g. figs. 6a, b**). Field data were collected from a total of 16 localities in Devon (**figs. 1c, 2**): 4 localities for the CHF (**figs. 4a-f)** and 12 localities for the HSF (**figs. 5a-d**), and are sedimentologically representative of each member of the SSG. The data collection approach and the palaeohydraulic workflow applied to this data build on the bedform-based method established by Ganti et al. (2019), Lyster et al. (2021), Wood et al. (2022), and McLeod et al. (2025) (**fig. 3**). There are uncertainties within all palaeohydraulic approaches, which include the bedform preservation ratio used within the workflow; the scaling relationship between bedform height and bankfull water depth; and the relationship between the bankfull water depth, sediment grain size and reconstructed palaeoslope. These need to

be appropriately propagated, and is done using a Monte Carlo approach (see below). In addition, we contextualise these palaeohydraulic data with outcrop-based observations of facies and architectural elements; these observations complement multiple previous facies analyses in these outcrops (Smith, 1990; Smith and Edwards, 1991; Lorsong and Atkinson, 1995; McKie and Williams, 2009; Newell, 2017b).

Measurements were made of maximum dune-scale cross-set thickness (n = 377) and cross-set thickness distributions (n = 51, **figs. 4f, 5h**): these measurements enable us to constrain typical subaqueous bedform sizes, which can be quantitatively linked to palaeoflow depths. Cross-set thicknesses were measured to a precision of 10 mm, with thickness distributions containing c. 10 evenly spaced measurements per cross-set. From cross-set distributions, the scaling relationship between mean and maximum cross-set thickness could then be derived. Maximum cross-set thicknesses were then transformed into synthetic mean thicknesses using this scaling factor, increasing the total number of mean cross-set thickness values to n = 428. Mean thicknesses were then incorporated into the palaeohydraulic workflow to calculate bankfull flow depths, using the scaling relationships of Leclair and Bridge (2001) and Bradley and Venditti (2017), with a Monte-Carlo approach to propagate uncertainty (cf. Lyster et al., 2021) (**fig. 3**). Measurements were also made of cross-set lee face dip and dip direction to constrain palaeocurrents (n = 231, **figs. 4f; 5h**).

Architectural observations and measurements were made of fluvial bars and simple channel-fill elements. In the SSG, barforms are often laterally and vertically amalgamated (**figs. 4a-d, 5a-f**), but can be recognised by inclined, low-angle accretion surfaces, often with superimposed higher angle dune cross-bedding (**figs. 4e, f, 5g, h**). The maximum thicknesses of bars and channel-fill architectural elements (n = 41) provide an independent constraint on minimum bankfull flow depth. Bar and channel-fill thicknesses were also measured using published, interpreted architectural panels (Localities A, B in **fig. 1a, 2,** Lorsong and Atkinson, 1995; Newell and Shariatipour, 2016), and from one cliff section at Danger Point (locality 7, **fig. 1a**). Measurements were also made of the dip and dip direction of barform accretion

surfaces (n = 97). When combined with palaeocurrent measurements, the accretionary style of bars (downstream, lateral and upstream) could be determined (e.g. Miall, 1994; 2006; Valenza et al., 2026). Rarely, inclined, barform lateral-accretion surfaces could be traced laterally and their length measured (n = 2) to provide constraints on bankfull channel width (Greenburg et al., 2022). All barform-scale architectural-element measurements of thickness and length were made using a laser range finder to a precision of 0.1 m.

Median grain size (D_{50}) was measured for both gravel-grade and sand-grade sediment (**figs. 6a, b**). For sandstone-dominated packages (D_{50} < 2 mm), D_{50} was measured by visual inspection using the grain-size classification of Wentworth (1922) (n = 67). For conglomeratic packages (D_{50} > 2 mm), D_{50} was obtained by measuring the long axis of clasts using the method of Wolman (1954). Measurements of gravel-grade sediment were made to a precision of 1 mm, both in the field and from outcrop photographs (n = 19, 100 measurements each). Median grain size, along with calculated bankfull flow depths, was incorporated into the palaeohydraulic workflow to calculate palaeoslope (Trampush et al., 2011) (**fig. 3**).

3.2. Reconstruction of bankfull flow depth and slope

Dune-scale cross-set and barform-scale architectural-element thickness data for the SSG were decompacted using the procedure of Long (2021), using a mean compaction factor of 1.16 calculated from 14 individual thin sections collected from the field area (Burley 1987). Grain size data, along with decompacted cross-set and architectural-element thickness data, were then grouped by lithostratigraphic division. This grouping allows temporal changes in palaeohydraulic character to be appraised.

For each lithostratigraphic division, dune-scale thickness, architectural-element-scale thickness and grain size data were passed through a series of scaling relationships to derive successive palaeohydraulic parameters. Where relationships have stated uncertainties, a Monte Carlo uncertainty propagation was used to produce statistically robust results, with 10^5

outcomes modelled with a rectangular distribution within the bounds of respective uncertainties.

Firstly, original dune heights (h_d) were calculated from mean decompacted cross-set thicknesses (h_{xs}), using **Equation 1** (Leclair and Bridge, 2001), where h_d is a function of h_{xs}. The relationship implies an h_d to h_{xs} scaling factor of 2.9 (equivalent to a bedform preservation ratio of c. 0.34), with the uncertainty of ± 0.7 representing the standard deviation of their dataset. This equation is ultimately derived from the theoretical work of Paola and Borgman (1991), and is appropriate for bedforms migrating over random topography with a negligible angle of climb.

$$h_d = (2.9 \pm 0.7)h_{xs} \quad \textbf{(1)}$$

Bankfull flow depths (H) were calculated from h_d using a compilation of flume tank and observational data from sand bed modern rivers (Equation 2) (Bradley and Venditti, 2017). This relationship implies an h_d to H scaling factor of 6.7, with lower and upper bounds of 4.4 and 10.1 representing a prediction interval of 50%.

$$H = (6.7^{+3.4}_{-2.3})h_d \quad \textbf{(2)}$$

H was also independently reconstructed from the maximum decompacted vertical thicknesses of accretionary barform and simple channel-fill architectural elements (h_{bar}). Bars in the SSG are often vertically amalgamated and truncated, so values of h_{bar} represent minimum estimates (**fig. 4a-d, fig. 5a-f**). The results of barform and dune-scale approaches were then compared to ensure that results were consistent and geologically reasonable.

Palaeoslopes (S, m/m) were calculated using the relationship of Trampush et al. (2014) (**Equation 3**), which in effect is a semi-empirical solution for bankfull Shields stress as a function of particle Reynolds number. Here, S is expressed a function of H and D_{50}, with parameters derived using a global database of both sand- and gravel-bed modern rivers. Uncertainties in coefficients in **Equation 3** represent the standard deviation of uncertainty from the compiled dataset of Trampush et al. (2014).

263 $$\log S = (-2.08 \pm 0.036) + (0.254 \pm 0.016) \log D_{50} + (-1.09 \pm 0.044) \log H \quad \textbf{(3)}$$

264

265 ### 3.3. Constraining fluvial planform and width

266 Constraints on fluvial planform are important for creating accurate depositional models
267 and evaluating the response of rivers to external forcings, such as climate and tectonics (e.g.
268 Galeazzi, 2021; Lyster et al., 2022 Wood et al., 2025; Mcleod et al., 2025). Estimates of total
269 active channel width, *W*, are required to obtain total bankfull water and sediment flux values
270 for sediment routing system reconstruction (see below). *W* is also important for the
271 palaeohydraulic workflow, as width is commonly used to interpret planform (Parker, 1976;
272 Ganti et al., 2019; Lyster et al., 2022; Wood et al., 2022; McLeod et al., 2025). However, *W*
273 cannot be directly measured as the SSG is largely composed of channel-fill bodies that are
274 incompletely preserved due to erosional truncation within multistorey, multilateral channel-fill
275 complexes. Considering this uncertainty, we reconstruct fluvial planform using both the results
276 of palaeohydraulic methods, and our facies and architectural observations. We then
277 reconstruct plausible values of *W* for each stratigraphic division of the SSG by comparing our
278 interpreted fluvial planforms, bed grain size and palaeohydraulic parameters *H* and *S* to similar
279 modern rivers with known *W/H* ratios. The accuracy of *W* is further tested with reference to
280 generalised, globally derived scaling relationships relating *W* and *H* (Galeazzi et al., 2021;
281 Long et al., 2021; Greenberg et al., 2021).

282 The first method to constrain planform was an evaluation of the bar-dune angular
283 difference (Δ_{db}, °) recorded by fluvial stratigraphy. Δ_{db} is calculated for each bar accretion
284 package as the angle between the mean bar accretion direction relative to dune palaeoflows.
285 For each stratigraphic division, bars are classified as downstream accreting (Δ_{db}<45°), laterally
286 accreting (45°<Δ_{db}<135°) or upstream accreting (135°<Δ_{db}<180°). Rivers dominated by
287 downstream accreting bars have low-sinuosity channels and are multi-threaded, whereas
288 lateral accretion is prevalent in rivers with high-sinuosity channels. These rivers can be either
289 single-threaded or multi-threaded (Bristow and Best, 1993; Bridge, 1993; Miall, 1994; Galeazzi

et al., 2021). Our interpretations of fluvial planform were further combined with observations of facies-scale and architectural-element scale sedimentology, allowing us to identify braided, anastomosing and meandering planform endmembers. We recognise that planform definitions are inconsistent for anastomosing rivers (e.g. Nanson and Knighton, 1996; Makaske, 2001; Carling et al., 2014). We describe anastomosing rivers using the discriminator of Lyster et al. (2022), in which they are defined as multi-threaded rivers with stable bars.

To derive *W/H* for each stratigraphic division, the rivers of the HSF are compared to a database of sand bed modern rivers in the Kati Thanda-Lake Eyre Basin, Australia, as these modern systems are argued to be sedimentologically and climatically analogous to the SSG and time-equivalent deposits across NW Europe (Brookfield, 2008; McKie, 2014; Morón et al., 2014; English et al., 2024). For the CHF, we compare our results to the global modern dataset of Lyster et al. (2022), in the absence of recognised direct analogues. By identifying a suite of modern rivers with a comparable bed grain size, planform, *H* and *S*, we can extract geologically plausible values of *W/H* for the rivers of the SSG.

Where possible, we reference our resulting values of *W/H* to the globally generalised, combined scaling relations of Long (2021) and Galeazzi et al. (2021), and the scaling relation of Greenberg et al. (2022), applied to fully preserved laterally accreting bar surfaces. These scaling relations are detailed in **Supplementary Material 1**.

3.4. Unit and bankfull water discharge and sediment flux

Firstly, flow velocity (*U*, m/s) was calculated using the equation of Manning et al. (1890) (**Equation 4**). *U* is a function of *H*, *S,* and the roughness coefficient *n*, set to 0.04 ± 0.01. This value is recommended for channels containing gravel to cobble-grade sediment (Chow, 1959), as in the CHF. In the HSF, *n* reflects roughness values for modern sand-bedded dryland river channels, which are vegetated to varying degrees (e.g. Tooth and Nanson, 2004; Bullard et al., 2007; Sandercock et al., 2007; Nanson and Huang, 2017). Unit water discharge

($Q_{w,u}$, m²/s), water discharge per unit width, can then be calculated by multiplying U by H (**Equation 5**).

$$U = \frac{1}{n} H^{1.5} S^{0.5} \quad \textbf{(4)}$$

$$Q_{w,u} = UH \quad \textbf{(5)}$$

Bankfull water discharge for the entire system ($Q_{w,bf}$, m³/s) is calculated by multiplying unit water discharge ($Q_{w,u}$) by W, the total active channel width.

Bankfull sediment flux for the entire system ($Q_{w,\,bf}$, kg/s) is calculated from W and unit sediment flux ($Q_{s,u}$, kg/m/s). Although there are numerous methods for calculating $Q_{s,u}$ (e.g. Barry et al., 2004; Jacobs, 2022; Martin-Moreta et al., 2023), we use the method of Meyer-Peter and Müller (1948), modified by Wong and Parker (2006) to calculate bedload transport, and the method of Engelund and Hansen (1967) for suspended bedload transport. These methods are appropriate for our needs because they incorporate our palaeohydraulic parameters without additional inputs, and have been used effectively to calculate sediment flux in the geological past (Sharma et al., 2023; McLeod et al., 2025).

The method of Meyer-Peter and Müller (1948), modified by Wong and Parker (2006) gives $Q_{s,u}$ for bedload transport as:

$$Q_{s,u} = \rho_s \left(g {D_{50}}^3 \Delta\rho\right)^{0.5} C(\tau_{*b} - \tau_{*c})^{\alpha} \quad \textbf{(6)}$$

In **Equation 6**, ρ_s is the density of sediment, 2600 kg/m³, g is gravitational acceleration, 9.81m/s², and $\Delta\rho$ is the dimensionless submerged specific gravity of sediment, 1.6. Constants C and α are 4.93 and 1.6 respectively. τ_{*c} is the dimensionless critical shear stress, given as a range between 0.03 and 0.06, reflecting measurements taken from modern gravel-bed rivers (Peitit et al., 2015). τ_{*b} is the dimensionless bed shear stress, and is given as:

$$\tau_{*b} = \frac{HS}{\Delta\rho D_{50}} \quad \textbf{(7)}$$

The method of Engelund and Hansen (1967) gives $Q_{s,u}$ for the suspended part of the bedload as:

$$Q_{s,u} = \rho_s \left(g {D_{50}}^3 \Delta\rho\right)^{0.5} q_{*t} \quad \textbf{(8)}$$

In **Equation 8**, q_{*t} is the dimensionless Einstein number, which relates shear stress and bed friction. For an extended methodology, see **Supplementary Material 1**. For sand bed rivers, we calculate sediment flux using **Equation 6**. For gravel-bed rivers, we calculate sediment flux by summing the results of **Equation 6** and **Equation 8**.

4. Results

4.1. Lithofacies character

Previous studies of the Devon coastal section of the SSG have documented lithofacies character and architecture in detail (Smith, 1990; Smith and Edwards, 1991; McKie and Williams, 2009; Newell, 2017b). We do not repeat this work here: instead we provide an overview focused on key observations to support our quantitative palaeohydraulic analyses.

Conglomerates in the CHF are clast-supported, structureless to imbricated, and have clast sizes of pebble to cobble grade in a matrix of coarse-grained sandstone. Clasts are rounded to well-rounded, and are composed mainly of quartzite (**fig. 4e-f, 6a)**. Clast size distributions are similar for the lower and upper CHF, with the former having a D_{16} of 19 mm, D_{50} of 40 mm and D_{84} of 85 mm, and the latter a D_{16} of 20 mm, D_{50} of 40 mm and D_{84} of 95 mm. Dune-scale cross-stratification is comparatively rare due to the coarse grain size of the CHF, but is 3-10 cm thick where present. In the HSF, conglomerates are clast-supoorted, dominantly granule- and pebble-grade, with clast shapes ranging from well-rounded to subangular. These facies are assigned codes codes Gm, Gt and Gl by Lorsong and Atkinson (1995). Conglomerates are composed of extraclasts of vein quartz, quartzite and fine-grained volcanics, intraclasts of rhizocretions and mudstone, and are frequently cemented by calcite (**fig. 6e, f**). These conglomerates range from structureless to cross-bedded, with sets 0.03-0.12 m thick. Conglomerate facies were deposited by the subaqueous, tractional bedload transport of gravel, with rare, poorly developed dunes in the CHF, but better developed dunes in the finer-grained HSF.

368 Sandstones are red-brown to orange, and range from structureless to cross-bedded.
369 Both planar and trough cross-bedding are present. These facies are assigned codes Sp, Sl,
370 Ss and St by Lorsong and Atkinson (1995). Grain size generally ranges between fine and
371 medium sand, sorting between poor and well-sorted, and sandstones locally contain stringers
372 and lag deposits of small pebbles and granules (**figs. 4e, f, 5g, h**). Cross-sets are generally
373 0.03-0.12 m thick, and both high- and low-angle cross-stratification are observed: dune lee-
374 face angles range from 6° to 34°. The abundance of dune-scale cross-bedded sandstone
375 indicates deposition by straight and sinuous-crested dunes migrating under unidirectional,
376 subaqueous flow.

377 In the SSG, dune palaeoflow data record north- and northeast-directed palaeocurrents
378 (**Supplementary Material 1**). These measurements build on previously collected
379 palaeocurrent data (Sellwood et al., 1984; Smith and Edwards, 1991; Benton et al., 1993;
380 Lorsong and Atkinson, 1995; Hart, 2014; Newell, 2017b), but increase the volume of data
381 reported for the CHF by a factor of >8 (Smith and Edwards, 1991), and increase the spatial
382 range of data in the HSF (Newell, 2017b; **Supplementary Material 1**). The collection of new
383 palaeocurrent data also allows dune palaeoflows to be linked with bar accretion direction to
384 appraise Δ_{db}, a key parameter for characterising river planform.

385 Mudstones are red-brown or green, and are structureless to laminated. Heterolithic
386 strata are composed of cm-scale interbedded mudstone, and fine- and very fine-grained
387 sandstone which may show planar lamination or cross-lamination (**fig. 5e, f**). These facies
388 have previously been represented by codes Fm and Fl, and Hl, respectively (Lorsong and
389 Atkinson, 1995). Both lithofacies locally contain bioturbation. Mudstone facies were deposited
390 subaqueously from suspension, whereas heterolithic facies record variations of flow velocity
391 and sand supply, with sandstones being deposited by shallow, unidirectional currents.
392

393 ### 4.2. Lithofacies architecture

In the CHF, conglomeratic lithofacies are arranged into vertically and horizontally amalgamated architectural elements 0.5-4.0 m thick, separated by inclined to subhorizontal erosional boundaries; these elements are interpreted as bar deposits (**fig. 4a-d**). Bar deposits range from structureless to having well-developed cross-stratified bar-scale sets. Each bar-scale set is normally graded, or contains dune-scale cross-bedding oriented subparallel or nearly perpendicular to the inclined erosional surface defining the lateral margin of an element, respectively indicating downstream and lateral bar accretion. The CHF also contains a subset of sandstone-dominated bars with poorly to well-developed bar-scale stratification, with each bar set containing cross-bedded sandstone lithofacies (**figs. 4a-d)**. The architecture of bar elements in the lower and upper CHF are notably different. Bar elements in the lower CHF are laterally extensive (>30 m), with steeply inclined erosional boundaries and bar cross-strata suggesting deposition in deep, confined channels (**fig. 4a, b**). In contrast, bar elements in the upper CHF are thinner, erosional boundaries are shallower in inclination and depth, and sandstone lithofacies are more common (**fig. 4c, d**). Mudstone and heterolithic lithofacies are absent in the CHF.

The HSF is dominated by horizontally and vertically amalgamated sandstone architectural elements 0.3-3.9 m thick, which are bounded by concave-up, shallowly inclined or subhorizontal erosional surfaces. These architectural elements are interpreted as bar deposits. Bar deposits are dominated by massive and cross-bedded sandstone lithofacies, and locally contain a 0.05-0.2 m thick basal bed of conglomerate lithofacies (**figs 5a-f**). Contacts between lithofacies are often sharp. Bar-scale cross-stratification, from the base to the top of an element, is moderately to well-developed. Both high-angle and low-angle bar stratification is observed, and set dip angles range between 3° and 30°. Bar elements have three main geometries. Simple, sheet-like bar elements with shallowly inclined to subhorizontal bounding surfaces, between which bar-accretion surfaces are subparallel to dune-scale palaeocurrents, are interpreted as downstream-accreting bar deposits (**figs. 5a-d)**. Lenticular elements with a subhorizontal upper bounding surface and an erosional, concave-upward lower bounding surface are interpreted as channel cut-and-fill deposits (**figs.**

5c-f). Bar elements with gently dipping bounding surfaces and inclined, large-scale cosets oriented perpendicular to dune-scale cross-bedding are interpreted as laterally accreting bar deposits (**figs. 5e, f**). Rarely, bar elements are also overlain by mudstone-dominated strata, which are generally less than 1 m in thickness. These are interpreted as fluvial overbank and channel abandonment deposits (**fig. 5e, f**). Conglomerate lithofacies are also found in 1-2 m thick, laterally extensive carbonate-cemented sheets overlying planar erosion surfaces at least 30-50 m in extent. The largest conglomerate sheet at Ladram Bay (locs. 8,9, **fig. 1c**) extends for up to a kilometre, and its erosional base may represent a channel-belt boundary (Lorsong and Atkinson, 1995).

Clear changes in lithofacies architecture occur through the HSF. The Otterton Ledge Member is dominated by simple, sheet-like, downstream accreting bar elements (**fig. 5a, b**). Bar elements in the Chiselbury Bay Member are generally thicker, wider, and more architecturally diverse: downstream accreting elements occur with a subset of laterally accreting elements and channel fills, which are >5 m wide and have 1.5-4 m of basal erosional relief (**fig. 5c, d**). In the Pennington Point Member, laterally accreting bar elements and channel-fill elements are interbedded with fluvial overbank successions 0.3-2 m thick (**fig. 5e, f**). Fluvial bar and channel-fill deposits, and overbank deposits exist in roughly equal proportions.

Throughout the HSF, the upper parts of bar-accretion and channel-fill elements are commonly overprinted by horizons of subvertical pedogenic rhizocretions (**fig. 6c, d**): calcite nodules precipitated by phreatophytic vegetation (Purvis and Wright, 1991; Newell, 2017b). Reworked rhizocretions also occur in lag deposits at the base of channel bodies (**fig. 6e, f**). They are found in all three studied units, but are most common in the Otterton Ledge Member (**fig. 6c**). *In situ* rhizocretions generally have maximum lengths of 1-2 m, but are recorded to reach several metres (Purvis and Wright, 1991). Their abundance suggests that the fluvial landscape was vegetated and the climate was semi-arid during the mid-Triassic.

4.3. Bankfull flow depths

From our dune-scale cross-set distributions, we identify a linear relationship between maximum cross-set height and mean height in the SSG with a coefficient of 0.6 and a coefficient of determination (r^2) of 0.962 (**fig. 7a**). This relationship is comparable to the results of previous studies (Lyster et al., 2021; Wood et al., 2022; Mcleod et al., 2025), suggesting that our cross-set scaling method is reliable. A Cumulative Distribution Function of reconstructed mean cross-set heights for the CHF is presented in **Figure 7b**. Median reconstructed cross set heights are 0.065 m for the lower CHF, and 0.070 m for the upper CHF (n = 23 and 25 respectively, **fig. 7b**). In the HSF, median cross set heights are 0.060 m for the Otterton Ledge Member, 0.075 m for the Chiselbury Bay Member, and 0.090 m for the Pennington Point Member (n = 114, 156 and 110 respectively, **fig. 7c**). These values imply that, for a bedform preservation ratio of 0.34 ± 0.07 (Leclair and Bridge, 2001), subaqueous dunes on the base of rivers had median heights of 0.19 ± 0.05 m in the lower CHF, and median heights of 0.21 ± 0.05 m in the upper CHF (**fig. 7b**). In the HSF, subaqueous dunes had median heights of 0.17 ± 0.04 m in the Otterton Ledge Member, 0.22 ± 0.05 m in the Chiselbury Bay Member, and 0.26 ± 0.06 m in the Pennington Point member (**fig. 7c**).

Bankfull flow depths (H) obtained using our bedform-based approach (**equations 1, 2**) range between 0.5 and 4.0 m (**fig. 8**). Significantly, for each stratigraphic division except the lower CHF, bedform-derived values of H are similar to values of H obtained from the thicknesses of bar-accretion architectural elements, confirming that these approaches are broadly consistent in estimating palaeo-flow depths (**fig. 8**). The dominantly conglomeratic lower CHF is an exception: H calculated from the bedform-based approach ranges between 0.8-2.8 m, whereas H calculated from barform-based measurements ranges between 2.1-4.6 m (**fig. 8**). This discrepancy arises because flow conditions and grain size lie at the margins of the dune stability field for coarse gravel-bed rivers such as the CHF (Dade and Friend, 1998). Consequently, dunes are often absent and those observed are unlikely to record flow conditions in the largest channel threads.

476 Accordingly, for the lower CHF, values of *H* derived from the barform-based approach
477 are propagated into the Monte Carlo workflow using a triangular distribution (n = 10^5) with a
478 minimum of 2 m, a maximum of 6 m, and a mode of 2.5 m. For all other units, our statistically
479 robust bedform-based results are propagated.
480 For the HSF, Mood's median (MM) tests and two-sample Cramer-von Mises (CvM)
481 tests show that the median and distribution of mean cross-set heights between each member
482 are both different to a confidence level of 98%. Furthermore, MM tests and CvM tests show
483 that the medians and distribution of h_{bar} are both statistically different between the upper and
484 lower CHF to a confidence level of 100%. Collectively, this suggests that cross-sets and
485 architectural elements were deposited by rivers with differing hydraulic characteristics.
486 Bankfull flow depths (p_{10}, p_{90}) in the Olenekian-aged CHF were initially 2.4-4.8 m, with
487 a median of 3.4 m (**fig. 9a**). Flow depths decreased to 1.2-2.0 m with a median of 1.7 m in the
488 upper half of the unit. In the Anisian-Ladinian aged HSF, flow depths appear to have increased
489 over time. For the Otterton Ledge Member, which represents much of the temporal range of
490 the HSF (**fig. 9a**), estimated flow depths were 1.0-2.0 m, with a median of 1.4 m. In the
491 Chiselbury Bay Member, bankfull flow depths then increased to 1.2-2.5 m, with a median of
492 1.8 m. In the Pennington Point Member, reconstructed flow depths were 1.4-3.0 m, with a
493 median of 2.1 m (**fig. 9a**). CvM tests show that distributions of *H* obtained for each time interval
494 are statistically different to a confidence level of 100%. MM tests also indicate that in all cases,
495 median values of *H* are distinct to a confidence level of 100%.
496

497 ### 4.4. Grain size and palaeoslope

498 In the conglomeratic CHF, the D_{50} grain size of clasts is 40 mm for both intervals.
499 Sandstones in the HSF are dominantly medium- and coarse-grained (**fig. 6b**), with granule
500 and pebble-grade lag deposits locally observed (**fig. 6e, f**). Overall, median grain sizes are
501 0.43 mm for the Otterton Ledge Member, 0.35 mm for the Chiselbury Bay Member, and 0.34
502 mm for the Pennington Point Member.

503 Calculated palaeoslopes (*S*) are a function of bankfull flow depths (**fig. 9a**) and D_{50}
504 grain size (**Equation 3,** Trampush et al., 2011). In the CHF, the median palaeoslope was
505 initially 1.0×10^{-3} m/m (i.e. 0.1%), and doubled to 2.0×10^{-3} m/m in the upper half of the unit
506 (**fig. 9b**). In the HSF, median palaeoslopes progressively decreased through time (**fig. 9b)**:
507 slope was initially 7.8×10^{-4} m/m in the Otterton Ledge Member, then 5.8×10^{-4} m/m in the
508 Chiselbury Bay Member, and finally 5.0×10^{-4} m/m (i.e. 0.05%) in the Pennington Point
509 Member. CvM tests and MM tests show respectively that both the statistical distribution and
510 median palaeoslope for all time intervals are different to a confidence level of 100%.

511

512 ### 4.5. Fluvial planform

513 Fluvial channel sinuosity was inferred from the angular difference between bar
514 accretion direction and dune migration direction (Δ_{db}), and from lithofacies architectural
515 observations.

516 In the HSF, median values of Δ_{db} are 34° for the Otterton Ledge Member and 33° for
517 the Chiselbury Bay Member (**fig. 10**). These values are consistent with architectural
518 observations which suggest a prevalence of downstream accreting bars. As such, both units
519 broadly represent the deposits of low-sinuosity, multi-threaded rivers. However, a temporal
520 increase in the interquartile range of Δ_{db} from 48° to 75° (**fig. 10**) suggests channel sinuosity
521 increased over time, and is consistent with the presence of a subset of laterally accreting bars
522 in the Chiselbury Bay Member. Bar elements in the Pennington Point Member have a median
523 Δ_{db} of 86° (**fig. 10**). Architecturally, this uppermost unit is dominated by laterally accreting bars,
524 channel-fill elements and fluvial overbank deposits, suggesting this unit likely represents a
525 high sinuosity meandering system.

526 The abundance of pedogenic rhizocretions in the HSF indicates that bars were highly
527 vegetated (**figs 6a-f**). Given that modern calcretes require many hundreds to thousands of
528 years to form (Candy et al., 2005; Alonso-Zarza, 2018), bars were likely to have been stable

over prolonged periods of time. This strongly indicates that the multi-threaded, low sinuosity rivers of the Otterton Ledge and Chiselbury Bay Members were anastomosing according to the definition of Lyster et al. (2022), and that the Pennington Point Member represents meandering river deposits.

In the conglomeratic CHF, a paucity of observed dune-scale cross-sets prevents a full statistical analysis of data. However, Δ_{db} ranges from 1-108° in the lower CHF, and 1-115° in the upper CHF (**fig. 10**). The spread of values observed, including very low angular differences, strongly suggests that both downstream and lateral accreting bars are preserved, indicating that the rivers of the CHF were low sinuosity and multi-threaded. Detailed sedimentological and architectural evidence presented by Smith (1990) and Smith and Edwards (1991) suggest that the lower CHF represents wandering river deposits, and so are most consistent with an anastomosing planform, whereas the architecture of the upper CHF matches well with the Donjek River in Canada (Smith, 1990; Smith and Edwards, 1991), an exemplar braided river (Miall, 2006).

4.6. Total active channel width

For each stratigraphic division of the SSG, inferred planform (braided, anastomosing, meandering), bed grain size (sand, gavel), bankfull flow depth (*H*) and slope (*S*) were compared with modern rivers to find appropriate analogues. Values of *W/H* recorded for these modern rivers can be used to estimate total active bankfull channel width (*W*) for the SSG rivers.

Rivers of the CHF were compared against the global modern dataset of Lyster et al. (2022). For the lower CHF, the most similar modern gravel-bed rivers are between 1.6 and 6.8 m deep, and have slopes of 0.00035 - 0.0012 m/m (**fig. 11a**). For the upper CHF, similar gravel-bed rivers are between 0.52 and 1.9 m deep, and have slopes of 0.0015 - 0.0046 m/m (**fig. 11b**).

For the anastomosing Otterton Ledge and Chiselbury Bay members, comparable transects of the Marshall and Diamantina Rivers (Tooth and Nanson, 2004; Brunner, 2013; Nanson and Huang, 2017) contain reaches with median bankfull depths of 0.64-2.6 m, and slopes of 0.0013 and 0.00020 m/m (**fig. 11c, d**). These modern rivers are commonly described as anabranching (Tooth and Nanson, 2004; Brunner, 2013; Nanson and Huang, 2017), but are considered under the anastomosing planform endmember by Lyster et al. (2022). For the meandering Pennington Point Member, comparable reaches of the Diamantina River have bankfull depths of 4.1-4.2 m, and slopes of 0.00020 m/m (**fig. 11e**).

From these modern river analogues, *W/H* ratios were obtained. For gravel-bed rivers, anastomosing rivers comparable to the lower CHF have a median *W/H* of 97, whereas braided rivers comparable to the upper CHF have a median *W/H* of 217 (**fig. 12**). For the Otterton Ledge and Chiselbury Bay members of the HSF, the median *W/H* of comparable sand-bed anastomosing rivers is 223 (**fig. 12**). For the Pennington Point Member of the HSF, the median *W/H* of comparable sand-bed meandering rivers is 24 (**fig. 12**).

W/H results were validated by using the scaling relationships of Galeazzi et al. (2021) and Long (2021) (**Supplementary Material 1**). This method produces a median *W/H* value of 76 for the lower CHF, 203 for the upper CHF, and 24 for the Pennington Point Member of the HSF (**fig. 12**), consistent with the results above. For the meandering rivers of the Pennington Point Member, values of *W/H* derived by the architecturally-based scaling relationship of Greenberg et al. (2021) also fall within the range of values observed in comparable modern systems (**fig. 12**, **Supplementary Material 1**). Furthermore, interpreted planforms and corresponding values of W/H for the SSG match well with the planform-based *W/H* stability criterion taken from the global modern dataset of Lyster et al. (2022), which discriminates between single and multi-threaded rivers (**fig. 12**).

In summary, all methods of estimation suggest that median *W/H* ratios derived from comparable modern rivers for the SSG are geologically realistic. When combined with our results of *H* , these *W/H* values can be confidently used to estimate *W*. Median values of *W* in the lower and upper Chester Formation were 330 m and 370 m, respectively. For the HSF,

583 median *W* was 320 m in the Otterton Ledge Member, 400 m in the Chiselbury Bay Member,
584 and 50 m in the Pennington Point Member (**Supplementary Material 1**).
585
586 ### 4.7. Water and sediment discharge
587 Median unit water discharge ($Q_{w,u}$) was estimated at 6.0 m²/s for the lower CHF, and
588 2.8 m²/s for the upper CHF (**fig. 13a**). In the HSF, $Q_{w,u}$ increased over time. Median $Q_{w,u}$ was
589 initially 1.3 m²/s in the Otterton Ledge Member, increasing to 1.6 m²/s in the Chiselbury Bay
590 Member, and to 2.0 m²/s in the Pennington Point Member (**fig. 13a**).
591 Bankfull water discharges ($Q_{w,bf}$) for the entire system were calculated from $Q_{w,u}$ and
592 *W,* and were overall substantially higher for the CHF than the HSF. Median $Q_{w,bf}$ was 580 m³/s
593 in the lower CHF, and 610 m³/s for the upper CHF (**fig. 13b**). In the HSF, median $Q_{w,bf}$ was
594 290 m³/s for the Otterton Ledge Member, increasing to 360 m³/s for the Chiselbury Bay
595 Member. $Q_{w,bf}$ was substantially lower in the Pennington Point Member, at 48 m³/s (**fig. 13b**).
596 Unit sediment fluxes ($Q_{s,u}$) were consistent throughout the SSG. Median values of $Q_{s,u}$
597 in the conglomeratic CHF were 11.9 kg/m/s for the lower part of the unit, and 12.1 kg/m/s for
598 the upper part of the unit (**fig. 14a**). In the HSF, a median $Q_{s,u}$, of 11.5 kg/m/s was estimated
599 for the Otterton Ledge Member, and a median $Q_{s,u}$ of 11.7 kg/m/s was estimated for both the
600 Chiselbury Bay and Pennington Point Members (**fig. 14a**).
601 Bankfull sediment fluxes ($Q_{s,bf}$) for the entire system were calculated from $Q_{s,u}$ and *W*.
602 Median values of $Q_{s,bf}$ were 3940 kg/s for the lower CHF and 4530 kg/s for the upper CHF
603 (**fig. 14b**). Median values of $Q_{s,bf}$ were 3670 kg/s for the Otterton Ledge Member, and 4670
604 kg/s for the Chiselbury Bay Member (**fig. 14b**). $Q_{w\,bf}$ is substantially lower for the Pennington
605 Point Member, at 603 kg/s (**fig. 14b**).
606
607 # 5. Discussion

5.1. Changing fluvial character in the Lower and Middle Triassic

Through our palaeohydraulic workflow, we quantitatively reconstruct changing values of bankfull flow depth, slope, planform and water and sediment discharge for rivers of the SSG (**fig. 15**). Overall, the SSG can be divided between the gravel-bed rivers of the CHF, and the sand-bed rivers of the HSF.

Rivers in the lower CHF had median bankfull flow depths of 3.4 m and slopes of 1.0×10^{-3} m/m. These rivers were most consistent with an anastomosing planform, with bankfull water discharges of c. 580 m^3/s and sediment fluxes of up to 4000 kg/s (**fig. 15**). The rivers which deposited the upper CHF had median bankfull flow depths of 1.7 m – half that for the lower CHF – and slopes twice as steep. These systems were likely braided, with increases in bankfull water discharge and bankfull sediment flux of 5% and 15%, respectively (**fig. 15**). Previous assessments of flow depth, derived from architectural observations, suggest that bankfull depths were 2-6 m in the CHF (Smith, 1990; Smith and Edwards, 1991), consistent with our quantitative palaeohydraulic results (**fig. 9a**). Our results further show that the CHF, which had previously been considered a single lithostratigraphic unit, is best considered as having been deposited by two distinct types of river with differing lithofacies architecture, bankfull flow depths, palaeoslopes and planforms. However, both have a similar gravel grain-size distribution and comparable bankfull water and sediment discharges (**fig. 14b; 15b**), suggesting that rivers had similar hydraulic conditions. The similarity of grain size and bankfull discharge, but difference in palaeoslope and planform suggests the change in fluvial style between the lower and upper CHF may have had a tectonic origin. However, a climatic origin, such as a change in bankfull discharge frequency, cannot be excluded. This change in fluvial style is likely recorded downstream of the Wessex Basin: a regional bipartite division of the CHF is also observed in the Worcester Graben and the Midlands Basins, 200-300 km north of the Wessex Basin (**fig. 1b,** Newell, 2017a).

In the HSF, the Otterton Ledge Member record rivers with median bankfull flow depths of 1.4 m and slopes of 7.8×10^{-4} m/m. These rivers broadly had an anastomosing planform,

635 with bankfull water discharges of 380 m³/s and sediment fluxes of 3670 kg/s (**fig. 15**). The
636 rivers of the Chiselbury Bay Member were c. 30% deeper than those of the Otterton Ledge
637 Member, with a c. 25% decrease in slope and c. 25% greater bankfull water discharge and
638 bankfull sediment flux. These rivers were also likely anastomosing, but had a greater number
639 of laterally accreting bars, and so a higher channel sinuosity (**fig. 15**). The rivers of the
640 Pennington Point Member had median depths of 2.1 m and slopes c. 13% lower than those
641 of the Chiselbury Bay Member rivers. The Pennington Point Member rivers were meandering,
642 with water discharges and sediment fluxes both c. 13% lower than those of the Chiselbury
643 Bay Member rivers. For the Chiselbury Bay Member of the HSF, Lorsong and Atkinson (1995)
644 and McKie and Williams (2009) estimated bankfull flow depths from lithofacies architectural
645 observations, yielding values of 4-5 m and 3 m, respectively. Our estimates of bankfull flow
646 depth for this member range between 1.2 and 2.5 m (p_{10} and p_{90} respectively, **fig. 8**), which
647 we systematically reconstruct from both bedform- and architectural-scale measurements. We
648 thus highlight the value of using quantitative approaches in accurately reconstructing channel
649 hydraulics (Wood et al., 2025).

650 Within the HSF, a general proximal-distal transition is observed, with rivers showing
651 decreasing grain size, decreasing slope and increasing sinuosity from base to top of the unit
652 (**figs. 9b, 10**). These trends illustrate the retreat and shortening of the Sherwood-2 River
653 System in response to the Muschelkalk transgression and coincident aridification (Bourquin et
654 al., 2011; McKie, 2017; Newell, 2017a; Yan et al., 2026). Our results further suggest that rivers
655 in the Chiselbury Bay Member record a brief (c. 1 Ma) time interval when rivers were deeper,
656 more sinuous and had greater bankfull discharges than the rivers in the Otterton Ledge
657 Member. A decrease in the abundance and size of pedogenic rhizocretions in the Chiselbury
658 Bay Member may indicate a higher water table and increased precipitation. These
659 interpretations are consistent with the depositional model of Newell (2017b), which suggested
660 that this unit represented a brief humid period during the middle Triassic. Finally, the rivers of
661 the Pennington Point Member record an abrupt eightfold decrease in bankfull water discharge

and sediment flux (**fig. 15**). These rivers, which we interpret as meandering in line with previous architectural interpretations (Lorsong and Atkinson, 1995; Svendsen and Hartley, 2001; Newell and Shariatipour, 2016), likely record the distal segment of the fluvial system. The decreases in bankfull water discharge and sediment flux observed likely originate from the transmission loss of water, and the division of the trunk system into several active distributary branches (**fig. 15, 16c,** Lang et al., 2004) where the Helsby Sandstone fluvial system discharged into the playa lake facies represented by the Mercia Mudstone Group (Howard et al., 2008).

Significantly, our results suggest that rivers in the Otterton Ledge and Chiselbury Bay Members were broadly anastomosing: lithofacies architecture and palaeohydraulic data suggests that these rivers were low-sinuosity and multi-threaded, whilst the abundance of pedogenic rhizocretions suggests that these rivers had vegetated, stable bars (**fig. 15**). This contrasts with previous interpretations of these units as braided river deposits (Sellwood et al., 1984; Purvis and Wright, 1991; Lorsong and Atkinson, 1995; Newell, 2017b; Coram et al., 2019). Estimated values of flow depth, slope, grain size and planform further suggest that these rivers in the HSF were comparable to modern dryland anastomosing (anabranching) rivers in Australia, such as the Marshall and Diamantina rivers (**figs. 11c-e, 16a, b**). These systems are sedimentologically and morphodynamically different from their humid counterparts (Nanson and Knighton, 1996; North et al., 2007). Humid zone anastomosing rivers are represented by isolated sandstone channel-fill bodies encased within fine-grained floodplain deposits (Nanson and Knighton, 1996; North et al., 2007; Wood et al., 2022; McLeod et al., 2025). In contrast, dryland anastomosing rivers are sand-dominated, contain complex anabranches and have wide channel belts (**fig. 16a, b,** Tooth and Nanson, 1999; Lang et al., 2004; North et al., 2007). These attributes appear consistent with our observations of the Otterton Ledge and Chiselbury Bay Members, further indicating that the HSF records an important example of dryland anastomosing rivers in the geological record.

5.2. Climate as a driver of river behaviour in the Sherwood Sandstone Group

Both the CHF and HSF were deposited in a climatically and tectonically dynamic setting (e.g. Bourquin et al., 2011; Radley and Coram, 2016; Newell, 2017a; b; Yan et al., 2026). In particular, the CHF is notable for its widespread distribution of conglomeratic lithofacies (Radley and Coram, 2016). Conglomeratic lithofacies persist into the British Midlands c. 300 km north of the Devon coastal section, and c. 400 km north of their source area (**fig. 1c,** e.g. Buist and Thompson, 1982; Steel and Thompson, 1983; Rees and Wilson, 1998). In contrast, similar source-to-sink systems draining from the Variscan mountains during the mid-Triassic and upper Carboniferous are characterised by sand-bedded rivers (Hallsworth et al., 2000; Wood et al., 2022; Yan et al., 2026). Any sediment sourcing control on the coarse grain size of this unit is unlikely: the well-rounded, dominantly quartzite clasts abundant in the CHF likely originate from the Gallic Massif in north France (**fig. 1a**; Plant et al., 1999; Sendino, 2012; Radley and Coram, 2015) rather than more proximal, local sources, where the pre-Triassic basement is largely sedimentary (**fig. 1c**, Yan et al., 2026).

The magnitude of hydrological change between the CHF and the HSF becomes apparent when our palaeohydraulic results are combined with catchment reconstructions and palaeoclimate constraints. Quantitative provenance analysis suggests that drainage length scales upstream of the Devon coastal section doubled to quadrupled between the CHF and HSF, from c. 100 km to 200-400 km (Morton et al., 2013), corresponding with a regional drainage organisation triggered by the Hardegsen tectonic event (e.g. Bourquin et al., 2011; von Eynatten et al., 2026). Using the geomorphic scaling relation of Nyberg et al. (2018), catchment areas are inferred to have been c. 1600 km² for the CHF, and 5800-20,000 km² for the HSF: increasing by a factor between 4 and 12. These contrast with our palaeohydraulic results, which show that bankfull water discharges in the CHF were double those of the HSF, and that sediment fluxes were comparable for both units. Effective daily precipitation, calculated from the ratio of bankfull water discharges and catchment areas of these systems, were c. 30 mm/day in the CHF, and c. 2-4 mm/day in the HSF, suggesting that precipitation

716 driving these discharge events was 7 to 20 times more intense in the early Triassic than the
717 middle Triassic. However, long-term runoffs were likely similar during both intervals: runoffs
718 of approximately 130 mm/y are reconstructed for the early Triassic (Ravida et al., 2021), and
719 100-250 mm/y for the middle Triassic, inferred from the presence of calcretes (**fig. 6c-f,** Eide
720 et al., 2018). These findings suggest that bankfull discharge events in the lower Triassic were
721 generated by intense but infrequent precipitation events, which also mobilised large amounts
722 of gravel grade material. This contrasts with the climatically stable middle Triassic, which
723 featured sand-bedded rivers active in a vegetated, faunally diverse landscape (e.g. Benton
724 and Newell, 2014; Radley and Coram, 2016; Newell, 2017a; b).

725 Evidence for a lower Triassic sedimentological perturbation can be correlated across
726 northwest Europe, and is marked in each basin by the appearance of a conglomerate sheet
727 extending hundreds of kilometres within a succession of mainly fluvial and aeolian sandstones
728 (e.g. Ramos et al., 1986; Bourquin et al., 2006; Durand et al., 2006). Like the CHF, these
729 conglomerates are texturally and compositionally mature, and are often capped by a ventifact
730 surface (e.g. Ramos and Sopena, 1983; Durand et al., 2006; Bourquin et al. 2006; 2007;
731 Costamagna, 2012). The rivers which laid down these deposits were fed from the same water
732 source: the Tethyan monsoon passing north over the remnant Variscan mountain belt (**fig. 1a;**
733 e.g. McKie, 2014; Ravida et al., 2021), and so likely had a similar hydrological regime to the
734 CHF rivers. The abrupt appearance of gravel-bed rivers across northwest Europe, which were
735 able to transport gravel-grade material over hundreds of kilometres (e.g. Plant et al., 1999;
736 Durand et al., 2006; Radley and Coram, 2016), coincident with a substantial perturbation in
737 the frequency and intensity of preciptiation, indicates a single, significant forcing during the
738 dynamic hothouse climate of the lower Triassic (**fig. 2**).

739 A rapid change in the hydraulic regime of rivers and a simultaneous increase in the
740 grain size of exported sediment is suggestive of sudden climate change (e.g. Armitage et al.,
741 2011; McLeod et al., 2024). Hyperthermal events in particular are associated with widespread
742 landscape devegetation, bedrock erosion and changes in precipitation regime. During the

743 Palaeocene-Eocene Thermal Maximum, rapid global warming of 5 °C over c. 270 kyr (Inglis
744 et al., 2020; Piedrahita et al., 2025) is well documented to have produced a coarsening of
745 fluvial sediment grain size, as well as extreme bankfull discharges from intensified precipitation
746 (e.g. Schmitz and Pujalte, 2007; Foreman et al., 2012; Carmichael et al., 2017; Van Praagh
747 et al., 2024; Prieur et al., 2025; Willard et al., 2026). Although tectonic forcings can also change
748 the grain size profile of rivers (e.g. Duller et al., 2010; Armitage et al., 2011; Whittaker et al.,
749 2011; Hampson et al., 2014; Reynolds, 2024), it is unlikely that substantial tectonic activity
750 contributed to the sedimentological changes observed in the CHF: palaeoslopes for this unit
751 (c. 1.0×10^{-3} m/m) are generally similar both to those for the HSF (c. 7.8×10^{-4} m/m, **fig. 9b**),
752 and to palaeoslopes recovered for the Carboniferous rivers of the Variscan foreland (c. $4.5 \times$
753 10^{-4}, Wood et al., 2022). Accordingly, we suggest the sedimentological and palaeohydraulic
754 character of the CHF is the signal of a lower Triassic hyperthermal.

755 The age of the CHF is constrained to the Olenekian Stage of the lower Triassic
756 (Hounslow et al., 2017). Correlation to coeval Triassic conglomerate sheets across northwest
757 Europe further suggests a probable Smithian age for these deposits (c. 250 – 248 Ma; Durand,
758 2006; Bourquin et al., 2011), indicating the most probable trigger for the development of highly
759 intermittent gravel-bed rivers was the Late Smithian Thermal Maximum (LSTM, Sun et al.,
760 2012; Lindström et al., 2019; Du et al., 2022; Armores et al., 2025). The LSTM was a c. 0.5
761 My-long hyperthermal triggered by activity from the Siberian Large Igneous Province (Du et
762 al., 2022), where continental temperatures, already elevated in the early Triassic, reached 35-
763 40°C (Sun et al., 2012). These extreme conditions triggered mass landscape devegetation at
764 low latitudes (Sun et al., 2012; Linström et al., 2019) and caused severe perturbations in the
765 global hydrological cycle (Linström et al., 2019). These effects are consistent with intense
766 bedrock erosion required to generate the abnormally coarse grain size of the CHF, as well as
767 the highly perturbed hydraulic regime interpreted: monsoonal weather systems are known to
768 be highly sensitive to climate change (Loo et al., 2015; Meijer et al., 2024).

In summary, our findings provide empirical, quantitative evidence of the low frequency, high-discharge hydraulic regime previously proposed for the lower Triassic (e.g. Gallois, 2014; Radley and Coram, 2016; Newell, 2017a), for which we argue that the LSTM was the most probable driver (**fig. 15**). More broadly, the CHF and associated deposits represent an isolated, intense episode of fluvial activity within a generally arid interval (e.g. Bourquin et al., 2011; Newell, 2017b). Sustained fluvial activity was only later established during the mid-Triassic (**fig. 15**; e.g. Ambrose et al., 2014; Newell, 2017a; b), with rivers being sourced by regular monsoonal precipitation under a relatively stable climate, evidenced by the abundance of vegetation and diverse biosphere (Benton et al., 2002; Dunhill et al., 2013; Coram et al., 2019). The regional association of lower Triassic conglomeratic sheets with the LSTM may not only provide a key stratigraphic constraint in a poorly resolved time interval, but provide insight into the continental response to a global, early Triassic hyperthermal which has hitherto proved difficult to identify and correlate.

6. Conclusions

The lower-to-middle Triassic Sherwood Sandstone Group, UK, comprises the deposits of dryland river systems which serve as a reservoir unit crucial for the energy transition, and record landscape evolution after the Permo-Triassic extinction. Through quantitative palaeohydrology and facies-based sedimentological observations of a complete section of the Sherwood Sandstone Group in Devon, southwest UK, we quantitatively reconstruct palaeoslopes, planforms, bankfull water discharges and bankfull sediment fluxes for these ancient rivers. In the conglomeratic Chester Formation, rivers were initially anastomosing and subsequently braided. Palaeoslopes were c. 1.0-2.0 × 10^{-3} m/m, bankfull water discharges were 580-610 m^3/s, and bankfull sediment fluxes were 3940-4530 kg/s. For most of the Helsby Sandstone Formation (c. 246.5-240.6 Ma), rivers were anastomosing, and were active under a stable, semi-arid climate, with clear evidence of palaeosols and vegetated, stable bars.

795 Bankfull water discharges were 290-360 m^3/s, and bankfull sediment fluxes were 3670-4670
796 kg/s.

797 From the base to the top of the Helsby Sandstone Formation, a clear proximal-to-distal
798 transition is observed. Palaeoslope progressively decreases through time, from 7.8×10^{-4} m/m
799 in the Otterton Ledge Member to 5.0×10^{-4} m/m in the Pennington Point Member,
800 accompanied by an increase in channel sinuosity. Furthermore, the palaeohydrology and
801 sedimentology of the meandering Pennington Point Member, in which an abrupt, eightfold
802 decrease in bankfull water discharge and bankfull sediment flux is observed, is consistent with
803 depositional models for a terminal splay system. Overall, these proximal-to-distal
804 palaeohydraulic and sedimentological trends were most likely caused by the Muschelkalk
805 marine transgression and synchronous regional aridification. The sedimentology, climate and
806 palaeohydrology of anastomosing and meandering rivers of the Helsby Sandstone Formation
807 indicate that they were comparable with the Marshall and Diamantina dryland rivers of the Kati
808 Thanda-Lake Eyre Basin, Australia. These systems, as well as other similar rivers, may serve
809 as suitable depositional analogues for sand-bedded rivers in the Sherwood Sandstone Group.

810 When the palaeohydrology of the Chester Formation and the Helsby Sandstone
811 Formation are integrated with catchment and palaeoclimate constraints, we estimate that
812 effective precipitation during the lower Triassic was likely 7-20 times more intense than that in
813 the mid-Triassic. However, long-term average precipitation remained comparatively constant
814 throughout, implying that changes in the frequency and magnitude of extreme rainfall events
815 may have influenced deposition in the lower Triassic CHF. The hydraulic characteristics and
816 coarse grain size of this unit suggest a perturbed hydrological cycle and widespread landscape
817 devegetation, which are consistent with the effects of a hyperthermal climatic event.
818 Sedimentological correlation across NW Europe suggest the c. 0.5 Myr-long Late Smithian
819 Thermal Maximum (c. 248 Ma) is a plausible driver behind the deposition of the Chester
820 Formation and other time-equivalent conglomerate units. We thus demonstrate the value of
821 quantitative palaeohydraulic methods, which use direct measurements of preserved fluvial

822 stratigraphy, in reconstructing climate signals in a palaeontologically barren, continental
823 setting.

824

825 7. Acknowledgements

826 We thank Andy Newell for insightful discussions about the SSG in Devon, and Jonah
827 McLeod for advice on applying quantitative palaeohydrological methods. We thank Ladram
828 Bay Holiday Park for granting us permission to access outcrops. Chris Fielding, an anonymous
829 reviewer and handling editor Frans van Buchem are thanked for providing comments which
830 helped improve this paper.

831

832 8. Funding statement

833 This work was funded by the Natural Environment Research Council (Grant NE/S007415/1).

834

835 9. Conflict of interest statement

836 The authors declare that they have no known competing financial interests or personal
837 relationships that could have appeared to influence the work reported in this paper.

838

839 10. Data Availability Statement

840 Data available in article supplementary material

841

842 11. References

Alonso-Zarza, A.M., 2018. Study of a modern calcrete forming in Guadalajara, Central Spain: An analogue for ancient root calcretes. *Sedimentary Geology*, *373*, pp.180-190. https://doi.org/10.1016/j.sedgeo.2018.06.006

Ambrose, K., Hough, E., Smith, N. J. P., and Warrington, G., 2014. Lithostratigraphy of the Sherwood Sandstone Group of England, Wales and south-west Scotland. British Geological Survey Research Report, RR/14/01.

Amores, M., Frank, T.D., Fielding, C.R., Hren, M.T. and Mays, C., 2025. Age-controlled south polar floral trends show a staggered Early Triassic gymnosperm recovery following the end-Permian event. *Geological Society of America Bulletin*, *137*(7-8), pp.3255-3282. https://doi.org/10.1130/B38017.1

Benton, M.J. and Newell, A.J., 2014. Impacts of global warming on Permo-Triassic terrestrial ecosystems. *Gondwana Research*, *25*(4), pp.1308-1337. http://dx.doi.org/10.1016/j.gr.2012.12.010

Benton, M.J. and Spencer, P.S. 1995. British Triassic fossil reptile sites. In: Fossil Reptiles of Great Britain. Springer, Dordrecht, https://doi.org/10.1007/978-94-011-0519-4_4

Benton, M. J., Warrington, G., Newell, A. J., and Spencer, P. S. 1994. A review of the British Middle Triassic tetrapod assemblages. In Fraser, N. C. and Sues, H.-D. (eds), In the shadow of the dinosaurs, pp. 131-160. Cambridge University Press, Cambridge, 435 pp.

Bhattacharya, J.P., Copeland, P., Lawton, T.F. and Holbrook, J., 2016. Estimation of source area, river paleo-discharge, paleoslope, and sediment budgets of linked deep-time depositional systems and implications for hydrocarbon potential. *Earth-Science Reviews*, *153*, pp.77-110. https://doi.org/10.1016/j.earscirev.2015.10.013

Blum, M.D. and Törnqvist, T.E., 2000. Fluvial responses to climate and sea-level change: a review and look forward. *Sedimentology*, *47*, pp.2-48. https://doi.org/10.1046/j.1365-3091.2000.00008.x

Bourquin, S., Peron, S. and Durand, M., 2006. Lower Triassic sequence stratigraphy of the western part of the Germanic Basin (west of Black Forest): fluvial system evolution through time and space. *Sedimentary Geology*, *186*(3-4), pp.187-211. https://doi.org/10.1016/j.sedgeo.2005.11.018

Bourquin, S., Durand, M., Diez, J.B., Broutin, J. and Fluteau, F., 2007. The Permian-Triassic boundary and lower Triassic sedimentation in western European basins: an overview. *Journal of Iberian Geology*, *33*(2), pp.221-236. https://doi.org/10.5209/JIGE.33912

Bourquin, S., Bercovici, A., López-Gómez, J., Diez, J.B., Broutin, J., Ronchi, A., Durand, M., Arché, A., Linol, B. and Amour, F., 2011. The Permian–Triassic transition and the onset of Mesozoic sedimentation at the northwestern peri-Tethyan domain scale: palaeogeographic maps and geodynamic implications. *Palaeogeography, Palaeoclimatology, Palaeoecology*, *299*(1-2), pp.265-280. https://doi.org/10.1016/j.palaeo.2010.11.007

Bradley, R.W. and Venditti, J.G., 2017. Reevaluating dune scaling relations. *Earth-science reviews*, *165*, pp.356-376. http://dx.doi.org/10.1016/j.earscirev.2016.11.004

Breeze, D., Scarselli, N., Hampson, G.J. and Chiarella, D., 2026. A review of multi-scale sedimentological heterogeneities in the Ormskirk Sandstone Formation of the East Irish Sea Basin and their impact on the injection and migration of CO2. *Journal of the Geological Society*, *183*(3), pp.jgs2025-099. https://doi.org/10.1144/jgs2025-099

Brémaud, M., Burnside, N.M., Shipton, Z.K., Bossennec, C., Fuchs, S. and Deon, F., 2026. How useful are outcrop samples to constrain subsurface thermal properties for geothermal exploration? Case study from the Chester formation, UK. *Geothermics*, *136*, p.103617. https://doi.org/10.1016/j.geothermics.2026.103617

Brookfield, M.E., 2008. Palaeoenvironments and palaeotectonics of the arid to hyperarid intracontinental latest Permian-late Triassic Solway basin (UK). *Sedimentary Geology*, *210*(1-2), pp.27-47. https://doi.org/10.1016/j.sedgeo.2008.06.003

Bridge, J.S., 1993. Description and interpretation of fluvial deposits: a critical perspective. *Sedimentology*, *40*(4), pp.801-810. https://doi.org/10.1111/j.1365-3091.1993.tb01361.x

Bristow, C.S. and Best, J.L., 1993. Braided rivers: perspectives and problems. *Geological society, London, special publications*, *75*(1), pp.1-11. https://doi.org/10.1144/GSL.SP.1993.075.01.01Brunner, P.R., 2013. Dryland Channel Forms and Processes: A Whole Catchment Scale Study of the Diamantina River, Central Australia. Doctoral dissertation, Griffith University. https://dx.doi.org/10.25904/1912/1345

900 Buist, D.S. and Thompson, D.B., 1982) Sedimentology, engineering properties and exploitation of
901 pebble beds in the Sherwood Sandstone Group (Lower Trias) of North Staffordshire with
902 particular reference to highway schemes. Mercian Geologist, 8, 241-269.
903 Bullard, J.E., Mctainsh, G.H. and Martin, P., 2007. Establishing stage-discharge relationships in
904 multiple-channelled, ephemeral rivers: A case study of the Diamantina river,
905 Australia. *Geographical Research*, *45*(3), pp.233-245. https://doi.org/10.1111/j.1745-
906 5871.2007.00457.x

907 Burgess, P.M., Dobromylskyj, E. and Lovell–Kennedy, J., 2025. Probably proximal pebbles? An
908 outcrop-constrained quantitative analysis of clast transport distances in the lower Triassic
909 Sherwood Sandstone Group, UK. *Journal of the Geological Society*, *182*(3), pp.jgs2024-155.
910 https://doi.org/10.1144/jgs2024-155

911 Burley, S.D., 1987. *Diagenetic modelling in the Triassic Sherwood sandstone group of England and its*
912 *offshore equivalents, United Kingdom continental shelf* (Doctoral dissertation, University of
913 Hull).

914 Candy, I., Black, S. and Sellwood, B.W., 2005. U-series isochron dating of immature and mature
915 calcretes as a basis for constructing Quaternary landform chronologies for the Sorbas basin,
916 southeast Spain. *Quaternary Research*, *64*(1), pp.100-111.
917 https://doi.org/10.1016/j.yqres.2005.05.002
918 Carling, P., Jansen, J. and Meshkova, L., 2014. Multichannel rivers: their definition and
919 classification. *Earth Surface processes and landforms*, *39*(1), pp.26-37.
920 https://doi.org/10.1002/esp.3419
921 Carmichael, M.J., Inglis, G.N., Badger, M.P., Naafs, B.D.A., Behrooz, L., Remmelzwaal, S., Monteiro,
922 F.M., Rohrssen, M., Farnsworth, A., Buss, H.L. and Dickson, A.J., 2017. Hydrological and
923 associated biogeochemical consequences of rapid global warming during the Paleocene-
924 Eocene Thermal Maximum. *Global and Planetary Change*, *157*, pp.114-138.
925 http://dx.doi.org/10.1016/j.gloplacha.2017.07.014

926 Castelltort, S., Fillon, C., Lasseur, É, Ortiz, A., Robin, C., Guillocheau, F., Tremblin, M., Bessin, P.,
927 Guerit, L., Dekoninck, A., Allanic, C., Gautheron, C., Barbarand, J., Loget, N., Uzel, J., Yans,
928 J., Briais, J., Al-Reda, M., Baby, G., François, T., Roig, J. & Calassou, S. (2023). The Source-

to-Sink Vade-mecum: History, Concepts and Tools. Society for Sedimentary Geology. CSP 16. http://doi.org/10.2110/sepmcsp.16

Chedburn, L., Underhill, J.R., Head, S. and Jamieson, R., 2022. The critical evaluation of carbon dioxide subsurface storage sites: Geological challenges in the depleted fields of Liverpool Bay. *AAPG bulletin*, *106*(9), pp.1753-1789. https://doi.org/10.1306/07062221120

Chow, V.T. 1959. Open-Channel Hydraulics. McGraw–Hill, New York.

Colombera, L., Mountney, N.P. and McCaffrey, W.D., 2013. A quantitative approach to fluvial facies models: Methods and example results. *Sedimentology*, *60*(6), pp.1526-1558. https://doi.org/10.1111/sed.12050

Coram, R.A., Radley, J.D. and Benton, M.J.. 2019 The Middle Triassic (Anisian) Otter Sandstone biota (Devon, UK): review, recent discoveries and ways ahead. Proceedings of the Geologists' Association, 130, 294–306, https://doi.org/10.1016/j.pgeola.2017.06.007

Costamagna, L.G., 2012. Alluvial, aeolian and tidal deposits in the Lower to Middle Triassic" Buntsandstein" of NW Sardinia (Italy): a new interpretation of the Neo-Tethys transgression. *Zeitschrift der Deutschen Gesellschaft fur Geowissenschaften*, *163*(2), p.165. https://doi.org/10.1127/1860-1804/2012/0163-0165

Dade, W.B. and Friend, P.F., 1998. Grain-size, sediment-transport regime, and channel slope in alluvial rivers. *The journal of Geology*, *106*(6), pp.661-676. https://doi.org/10.1086/516052

Downing, R.A., Allen, D.J., Barker, J.A., Burgess, W.G., Gray, D.A., Price, M. and Smith, I.F., 1984. Geothermal exploration at Southampton in the UK: a case study of a low enthalpy resource. *Energy exploration and exploitation*, *2*(4), pp.327-342. https://doi.org/10.1177/014459878400200404

Du, Y., Song, H., Algeo, T.J., Song, H., Tian, L., Chu, D., Shi, W., Li, C. and Tong, J., 2022. A massive magmatic degassing event drove the Late Smithian Thermal Maximum and Smithian–Spathian boundary mass extinction. *Global and Planetary Change*, *215*, p.103878. https://doi.org/10.1016/j.gloplacha.2022.103878

Duller, R.A., Whittaker, A.C., Fedele, J.J., Whitchurch, A.L., Springett, J., Smithells, R., Fordyce, S. and Allen, P.A., 2010. From grain size to tectonics. *Journal of Geophysical Research: Earth Surface*, *115*(F3). http://dx.doi.org/10.1029/2009JF001495

Dunhill, A.M., Benton, M.J., Newell, A.J. and Twitchett, R.J., 2013. Completeness of the fossil record and the validity of sampling proxies: a case study from the Triassic of England and Wales. *Journal of the Geological Society*, *170*(2), pp.291-300. https://doi.org/10.1144/jgs2012-025

Durand, M., 2006. The problem of the transition from the Permian to the Triassic Series in southeastern France: comparison with other Peritethyan regions. Geological Society, London, Special Publications, 265, 281–296. https://doi.org/10.1144/GSL.SP.2006.265.01.13

Eide, C. H., Müller, R. and Helland-Hansen, W. (2018) Using climate to relate water discharge and area in modern and ancient catchments. *Sedimentology.* 65 (4), 1378-1389. https://doi.org/10.1111/sed.12426.

Engelund, F. and Hansen, E., 1967. A monograph on sediment transport in alluvial streams.

English, K.L., English, J.M., Moscardini, R., Haughton, P.D., Raine, R.J. and Cooper, M., 2024. Review of Triassic Sherwood Sandstone Group reservoirs of Ireland and Great Britain and their future role in geoenergy applications. *Geoenergy*, *2*(1), pp.geoenergy2023-042. https://doi.org/10.1144/geoenergy2023-042

von Eynatten, H., Sass, K., Dunkl, I. and Schönig, J., 2026. Extension and clockwise shift of central to western Europe's drainage across the Permo-Triassic transition. International Journal of Earth Sciences, 115(3), p.32. https://doi.org/10.1007/s00531-026-02574-x

Fielding, C.R., Alexander, J. and Allen, J.P., 2018. The role of discharge variability in the formation and preservation of alluvial sediment bodies. Sedimentary Geology, 365, pp.1-20. https://doi.org/10.1016/j.sedgeo.2017.12.022

Foreman, B.Z., Heller, P.L. and Clementz, M.T., 2012. Fluvial response to abrupt global warming at the Palaeocene/Eocene boundary. Nature, 491(7422), pp.92-95. https://doi.org/10.1038/nature11513

Franklin, J., Tyrrell, S., O'Sullivan, G., Nauton-Fourteu, M. and Raine, R., 2020. Provenance of Triassic sandstones in the basins of Northern Ireland—Implications for NW European Triassic palaeodrainage. *Geological Journal*, *55*(7), pp.5432-5450. https://doi.org/10.1002/gj.3697

Galeazzi, C.P., Almeida, R.P.D. and Do Prado, A.H., 2021. Linking rivers to the rock record: Channel patterns and paleocurrent circular variance. *Geology*, *49*(11), pp.1402-1407. https://doi.org/10.1130/G49121.1

Gallois, R.W., 2014. The position of the Permo-Triassic boundary in Devon, UK. Geoscience in South-West England, 13, pp.328-338.

Ganti, V., Whittaker, A.C., Lamb, M.P. and Fischer, W.W., 2019. Low-gradient, single-threaded rivers prior to greening of the continents. Proceedings of the National Academy of Sciences, 116(24), pp.11652-11657. https://www.pnas.org/cgi/doi/10.1073/pnas.1901642116

Gasanzade, F. and Bauer, S., 2025. Subsurface potential in the German North Sea sector for geological carbon dioxide storage: new insights on capacity assessment. Environmental earth sciences, 84(12), p.340. https://doi.org/10.1007/s12665-025-12351-9

Greenberg, E., Ganti, V. and Hajek, E., 2021. Quantifying bankfull flow width using preserved bar clinoforms from fluvial strata. Geology, 49(9), pp.1038-1043. https://doi.org/10.1130/G48729.1

Hallsworth, C.R., Morton, A.C., Claoué-Long, J. and Fanning, C.M., 2000. Carboniferous sand provenance in the Pennine Basin, UK: constraints from heavy mineral and detrital zircon age data. *Sedimentary Geology*, *137*(3-4), pp.147-185. https://doi.org/10.1016/S0037-0738(00)00153-6

Hampson, G.J., Duller, R.A., Petter, A.L., Robinson, R.A. and Allen, P.A., 2014. Mass-balance constraints on stratigraphic interpretation of linked alluvial–coastal–shelfal deposits from source to sink: example from Cretaceous Western Interior Basin, Utah and Colorado, USA. *Journal of Sedimentary Research*, *84*(11), pp.935-960. http://dx.doi.org/10.2110/jsr.2014.78

Hart, M.B., 2014. The ‘Otter Sandstone River’of the mid-Triassic and its vertebrate fauna. *Proceedings of the Geologists' Association*, *125*(5-6), pp.560-566.http://dx.doi.org/10.1016/j.pgeola.2014.08.002

Henares, S., Donselaar, M.E. and Caracciolo, L., 2020. Depositional controls on sediment properties in dryland rivers: Influence on near-surface diagenesis. Earth-Science Reviews, 208, p.103297. https://doi.org/10.1016/j.earscirev.2020.103297

Hjelm, L., Anthonsen, K.L., Dideriksen, K., Nielsen, C.M., Nielsen, L.H. and Mathiesen, A., 2020. Evaluation of the CO2 storage potential in Denmark. *Danmarks og Grønlands Geologiske Undersøgelse Rapport*, *46*, p.2020.

Hossain, S., Hampson, G.J., Jacquemyn, C., Jackson, M.D. and Chiarella, D., 2024. Permeability characterisation of sedimentological facies in the Bunter Sandstone Formation, Endurance CO2 storage site, offshore UK. *International Journal of Greenhouse Gas Control*, *135*, p.104140. https://doi.org/10.1016/j.ijggc.2024.104140

Hounslow, M.W. and Gallois, R., 2023. Magnetostratigraphy of the Mercia Mudstone Group (Devon, UK): implications for regional relationships and chronostratigraphy in the Middle to Late Triassic of Western Europe. *Journal of the Geological Society*, *180*(4), pp.jgB2022-173. https://doi.org/10.1144/jgs2022-173

Hounslow, M.W., McIntosh, G., Edwards, R.A., Laming, D.J. and Karloukovski, V., 2017. End of the Kiaman Superchron in the Permian of SW England: magnetostratigraphy of the Aylesbeare Mudstone and Exeter groups. *Journal of the Geological Society*, *174*(1), pp.56-74. https://doi.org/10.1144/jgs2015-141

Hounslow, M.W. and McIntosh, G., 2003. Magnetostratigraphy of the Sherwood Sandstone Group (Lower and Middle Triassic), south Devon, UK: detailed correlation of the marine and non-marine Anisian. *Palaeogeography, Palaeoclimatology, Palaeoecology*, *193*(2), pp.325-348. https://doi.org/10.1016/S0031-0182(03)00235-9

Howard, A S, Warrington, G, Ambrose, K, and Rees, J G. 2008. A formational framework for the Mercia Mudstone Group (Triassic) of England and Wales. British Geological Survey Research Report, RR/08/04.

Inglis, G.N., Bragg, F., Burls, N.J., Cramwinckel, M.J., Evans, D., Foster, G.L., Huber, M., Lunt, D.J., Siler, N., Steinig, S. and Tierney, J.E., 2020. Global mean surface temperature and climate sensitivity of the early Eocene Climatic Optimum (EECO), Paleocene–Eocene Thermal

Maximum (PETM), and latest Paleocene. *Climate of the Past*, *16*(5), pp.1953-1968. https://doi.org/10.1016/j.ijggc.2024.104140

Jones, C.M. and Collinson, J.D., 2025. Discussion on 'Rivers of the Variscan Foreland: fluvial morphodynamics in the Pennant Formation of South Wales, UK' by Wood et al. 2022 (JGS, 180, jgs2022-048). Journal of the Geological Society, 182(5), pp.jgs2025-033. https://doi.org/10.1144/jgs2025-033

Lang, S.C., Payenberg, T.H.D., Reilly, M.R.W., Hicks, T., Benson, J. and Kassan, J., 2004. Modern analogues for dryland sandy fluvial-lacustrine deltas and terminal splay reservoirs. *The APPEA Journal*, *44*(1), pp.329-356. https://doi.org/10.1071/AJ03012

Leclair, S.F. and Bridge, J.S., 2001. Quantitative interpretation of sedimentary structures formed by river dunes. Journal of Sedimentary Research, 71(5), pp.713-716. https://doi.org/10.1306/2DC40962-0E47-11D7-8643000102C1865D

Leonard, A.J., AG, M. and EB, S., 1982. Ventifacts from a deflation surface marking the top of the Budleigh Salterton Pebble Beds, east Devon. Proceedings of the Ussher Society 5, 333.

Lindström, S., Bjerager, M., Alsen, P., Sanei, H. and Bojesen-Koefoed, J., 2020. The Smithian–Spathian boundary in North Greenland: implications for extreme global climate changes. *Geological Magazine*, *157*(10), pp.1547-1567. https://doi.org/10.1017/S0016756819000669

Long, D.G., 2021. Trickling down the paleoslope: an empirical approach to paleohydrology. *Earth-Science Reviews*, *220*, p.103740. https://doi.org/10.1016/j.earscirev.2021.103740

Loo, Y.Y., Billa, L. and Singh, A. (2015) Effect of climate change on seasonal monsoon in Asia and its impact on the variability of monsoon rainfall in Southeast Asia. Geoscience Frontiers, 6, 817–823. https://doi.org/10.1016/j.gsf.2014.02.009

Lorsong, J.A. and Atkinson, C.D., 1995. Sedimentology and stratigraphy of Lower Triassic alluvial deposits, East Devon coast. *Excursion guide. Petroleum Group. Geological Society, London*.

Lyster, S.J., Whittaker, A.C., Hampson, G.J., Hajek, E.A., Allison, P.A. and Lathrop, B.A., 2021. Reconstructing the morphologies and hydrodynamics of ancient rivers from source to sink: Cretaceous Western Interior Basin, Utah, USA. Sedimentology, 68(6), pp.2854-2886. https://doi.org/10.1111/sed.12877

Lyster, S.J., Whittaker, A.C. and Hajek, E.A., 2022. The problem of paleo-planforms. *Geology*, *50*(7), pp.822-826. https://doi.org/10.1130/G49867.1

Makaske, B., 2001. Anastomosing rivers: a review of their classification, origin and sedimentary products. *Earth-Science Reviews*, *53*(3-4), pp.149-196. https://doi.org/10.1016/S0012-8252(00)00038-6

McLeod, J.S., Whittaker, A.C., Hampson, G.J., Bell, R.E., Prieur, M., Fuller-Field, O.G., Valero, L., Yan, X. and Valenza, J.M., 2025. Hothouse Hydrology: Evolving River Dynamics in the Eocene Montllobat and Castissent Formations, Southern Pyrenees. *Basin Research*, *37*(5), p.e70059. https://doi.org/10.1111/bre.70059

McLeod, J.S., Wood, J., Lyster, S.J., Valenza, J.M., Spencer, A.R. and Whittaker, A.C., 2023. Quantitative constraints on flood variability in the rock record. Nature Communications, 14(1), p.3362. https://doi.org/10.1038/s41467-023-38967-8

McKie, T., 2011. A comparison of modern Dryland depositional systems with the Rotliegend group in the Netherlands. SEPM Special Publications. 98. 89-103. https://doi.org/10.2110/pec.11.98.0089.

McKie, T., 2014. Climatic and tectonic controls on Triassic dryland terminal fluvial system architecture, central North Sea. In: Martinius, A.W., Ravnås, R., Howell, J.A., Steel, R.J. and Wonham, J.P. (eds) From Depositional Systems to Sedimentary Successions on the Norwegian Continental Shelf. Blackwell, Oxford, 46, 19–58 [IAS Special Publication]. https://doi.org/10.1002/9781118920435.ch2

McKie, T., 2017. Palaeogeographic evolution of latest Permian and Triassic salt basins in Northwest Europe. In: Soto, J. I., Flinch, J. F. and Tari, G. (eds.) *Permo-triassic salt provinces of Europe, North Africa and the Atlantic margins* (pp. 159-173). Elsevier. https://doi.org/10.1016/B978-0-12-809417-4.00008-2

McKie, T. and Williams, B., 2009. Triassic palaeogeography and fluvial dispersal across the northwest European Basins. Geological Journal, 44(6), pp.711-741. https://doi.org/10.1002/gj.1201

Medici, G., West, L.J., Mountney, N.P. and Welch, M., 2019. Permeability of rock discontinuities and faults in the Triassic Sherwood Sandstone Group (UK): insights for management of fluvio-

aeolian aquifers worldwide. Hydrogeology Journal, 27(8), pp.2835-2855. https://doi.org/10.1007/s10040-019-02035-7

Meijer, N., Licht, A., Woutersen, A., Hoorn, C., Robin-Champigneul, F., Rohrmann, A., Tagliavento, M., Brugger, J., Kelemen, F.D., Schauer, A.J. and Hren, M.T., 2024. Proto-monsoon rainfall and greening in Central Asia due to extreme early Eocene warmth. *Nature Geoscience*, *17*(2), pp.158-164. https://doi.org/10.1038/s41561-023-01371-4

Meinshausen, M., Smith, S.J., Calvin, K., Daniel, J.S., Kainuma, M.L., Lamarque, J.F., Matsumoto, K., Montzka, S.A., Raper, S.C., Riahi, K. and Thomson, A.G.J.M.V., 2011. The RCP greenhouse gas concentrations and their extensions from 1765 to 2300. Climatic change, 109(1), p.213. https://doi.org/10.1007/s10584-011-0156-z

Menacherry, S., Kaldi, J., Lang, S. and Payenberg, T., 2009. PS Suitability of the Dryland Fluvial-Aeolian Sediments and Its Depositional System for CO2 Sequestration, Analogues Study from Umbum Creek, Lake Eyre, Central Australia. Presented at the AAPG International Conference and Exhibition, AAPG Search and Discovery, Cape Town, South Africa (2009), pp. 1-14

Meyer-Peter, E., and R. Müller. 1948. Formulas for Bed-Load Transport.

Miall, A.D. 1994. Reconstructing fluvial macroform architecture from two-dimensional outcrops; examples from the Castlegate Sandstone, Book Cliffs, Utah. Journal of Sedimentary Research, v. 64, p. 146-158.

Miall, A.D., 2006. The geology of fluvial deposits: sedimentary facies, basin analysis, and petroleum geology. Springer.

Mijnlieff, H.F., 2020. Introduction to the geothermal play and reservoir geology of the Netherlands. *Netherlands Journal of Geosciences*, *99*, p.e2. https://doi.org/10.1017/njg.2020.2

Millennium Ecosystem Assessment, 2005. Ecosystems and human well-being: wetlands and water synthesis. World Resources Institute, Washington, DC.

Morón, S., Amos, K. and Mann, S., 2014. Fluvial reservoirs in dryland endorheic basins: the Lake Eyre Basin as a world-class modern analogue. *The APPEA Journal*, *54*(1), pp.119-134. https://doi.org/10.1071/AJ13014

Morton, A., Hounslow, M.W. and Frei, D., 2013. Heavy-mineral, mineral-chemical and zircon-age constraints on the provenance of Triassic sandstones from the Devon coast, southern Britain. *Geologos*, *19*(1-2), pp.67-85. https://doi.org/10.2478/logos-2013-0005

Morton, A., Knox, R. and Frei, D., 2016. Heavy mineral and zircon age constraints on provenance of the Sherwood Sandstone Group (Triassic) in the eastern Wessex Basin, UK. *Proceedings of the Geologists' Association*, *127*(4), pp.514-526. https://doi.org/10.1016/j.pgeola.2016.06.001

Moscardini, R.I., English, K.L., Raine, R., Haughton, P.D., English, J.M. and Cooper, M., 2025. Reservoir heterogeneity in the Triassic Sherwood Sandstone Group: new insights from the Larne Basin, Northern Ireland. *Geoenergy*, *3*(1), pp.geoenergy2025-015. https://doi.org/10.1144/geoenergy2025-015

Nanson, G.C. and Huang, H.Q., 2017. Self-adjustment in rivers: Evidence for least action as the primary control of alluvial-channel form and process. Earth Surface Processes and Landforms, 42(4), pp.575-594. https://doi.org/10.1002/esp.3999

Nanson, G.C. and Knighton, A.D., 1996. Anabranching rivers: their cause, character and classification. *Earth surface processes and landforms*, *21*(3), pp.217-239. https://doi.org/10.1002/(SICI)1096-9837(199603)21:3%3C217::AID-ESP611%3E3.0.CO;2-U

Newell, A. J., 2017a. Rifts, rivers and climate recovery: A new model for the Triassic of England. *Proceedings of the Geologists' Association*, *129*(3), pp.352-371. https://doi.org/10.1016/j.pgeola.2017.04.001

Newell, A. J., 2017b. Evolving stratigraphy of a Middle Triassic fluvial-dominated sheet sandstone: The Otter Sandstone Formation of the Wessex Basin (UK). *Geological Journal*, *53*(5), pp.1954-1972. https://doi.org/10.1002/gj.3026

Newell, A. J., 2023 *The Sherwood Sandstone and Bacton groups of the East Midlands Shelf – an onshore to offshore correlation using outcrop evidence and geophysical logs.* Nottingham, UK, British Geological Survey.

Newell, A.J. and Shariatipour, S.M., 2016. Linking outcrop analogue with flow simulation to reduce uncertainty in sub-surface carbon capture and storage: an example from the Sherwood

Sandstone Group of the Wessex Basin, UK. *Geological Society, London, Special Publications*, *436*(1), pp.231-246. https://doi.org/10.1144/SP436

Newell, A J, Smith, N J., 2009. Bromsgrove Aquifer Groundwater Modelling Study: Results from Task 1.1 3D Visualisation and Geological Framework of the Bromsgrove Aquifer. British Geological Survey Commissioned Report, CR/09/023. 18pp.

North, C.P., Nanson, G.C. and Fagan, S.D., 2007. Recognition of the sedimentary architecture of dryland anabranching (anastomosing) rivers. *Journal of Sedimentary Research*, *77*(11), pp.925-938. https://doi.org/10.2110/jsr.2007.089

Nyberg, B., Helland-Hansen, W., Gawthorpe, R.L., Sandbakken, P., Eide, C.H., Sømme, T., Hadler-Jacobsen, F. and Leiknes, S., 2018. Revisiting morphological relationships of modern source-to-sink segments as a first-order approach to scale ancient sedimentary systems. *Sedimentary Geology*, *373*, pp.111-133. https://doi.org/10.1016/j.sedgeo.2018.06.007

Ogg, J. G., Chen, Z.-Q., Orchard, M. J., Jiang, H. S., 2020. Chapter 25 - The Triassic Period. In: Gradstein, F. M., Ogg, J. G., Schmitz, M. D., Ogg G. M., Geologic Time Scale, (pp. 903-953) Elsevier, https://doi.org/10.1016/B978-0-12-824360-2.00025-5.

Paola, C. and Borgman, L., 1991. Reconstructing random topography from preserved stratification. Sedimentology, 38(4), pp.553-565. https://doi.org/10.1111/j.1365-3091.1991.tb01008.x

Plink-Björklund, P., 2015. Morphodynamics of rivers strongly affected by monsoon precipitation: review of depositional style and forcing factors. *Sedimentary Geology*, *323*, pp.110-147. https://doi.org/10.1016/j.sedgeo.2015.04.004

Parker, G., 1976. On the cause and characteristic scales of meandering and braiding in rivers. Journal of fluid mechanics, 76(3), pp.457-480. https://doi.org/10.1017/S0022112076000748

Piedrahita, V.A., Heslop, D., Roberts, A.P., Rohling, E.J., Galeotti, S., Florindo, F. and Li, J., 2025. Assessing the duration of the Paleocene-Eocene Thermal Maximum. *Geophysical Research Letters*, *52*(7), p.e2024GL113117. https://doi.org/10.1029/2024GL113117

Plant, J. A., Jones, D. G., and Haslam, H W (editors). 1999. The Cheshire Basin: Basin evolution, fluid movement and mineral resources in a Permo-Triassic rift setting. Keyworth, Nottingham: for the British Geological Survey.

Van Praagh, C.J., Webb, J.A. and White, S.Q., 2024. The White Hills Gravel of central Victoria: an anomalous Paleogene very coarse-grained fluvial deposit. *Australian Journal of Earth Sciences*, *71*(6), pp.757-777. https://doi.org/10.1080/08120099.2024.2388575

Prieur, M., Robin, C., Braun, J., Vaucher, R., Whittaker, A.C., Jaimes-Gutierrez, R., Wild, A., McLeod, J.S., Malatesta, L., Fillon, C. and Schlunegger, F., 2025. Climate control on erosion: Evolution of sediment flux from mountainous catchments during a global warming event, PETM, Southern Pyrenees, Spain. Geophysical Research Letters, 52(7), p.e2024GL112404. https://doi.org/10.1029/2024GL112404

Purvis, K., Bird, A., Dempsey, E. and Hardman, K. 2025. U-Pb age dating of calcrete from the Triassic Helsby Sandstone Formation, South-East Devon: pilot study results. Proceedings of the Ussher Society, 15(4), 150–155.

Purvis, K. and Wright, V.P., 1991. Calcretes related to phreatophytic vegetation from the Middle Triassic Otter Sandstone of south west England. *Sedimentology*, *38*(3), pp.539-551. https://doi.org/10.1111/j.1365-3091.1991.tb00366.x

Radley, J.D. and Coram, R.A., 2015. Derived Skolithos pipe rock in the Budleigh Salterton Pebble Beds (Early Triassic, East Devon, UK). Proceedings of the Geologists' Association, 126(2), pp.220-225. http://dx.doi.org/10.1016/j.pgeola.2014.10.007

Radley, J.D. and Coram, R.A., 2016. The Chester Formation (Early Triassic, southern Britain): sedimentary response to extreme greenhouse climate?. *Proceedings of the Geologists' Association*, *127*(5), pp.552-557. http://dx.doi.org/10.1016/j.pgeola.2016.08.002

Ramos, A. and Sopeña, A., 1983. Gravel bars in low-sinuosity streams (Permian and Triassic, central Spain). *Modern and ancient fluvial systems*, pp.301-312. https://doi.org/10.1002/9781444303773.ch24

Ramos, A., Sopeña, A. and Perez-Arlucea, M., 1986. Evolution of Buntsandstein fluvial sedimentation in the northwest Iberian Ranges (Central Spain). *Journal of Sedimentary Research*, *56*(6), pp.862-875.

Ravidà, D.C., Caracciolo, L., Heins, W.A. and Stollhofen, H., 2021. Reconstructing environmental signals across the Permian-Triassic boundary in the SE Germanic basin: Palaeodrainage modelling and quantification of sediment flux. *Global and Planetary Change*, *206*, p.103632. https://doi.org/10.1016/j.gloplacha.2021.103631

Rees, J G, and Wilson, A A. 1998. Geology of the country around Stoke-on-Trent. Memoir of the Geological Survey, Sheet 123 (England and Wales).

Reynolds, T., 2024. Grain size from source to sink–modern and ancient fining rates. *Earth-Science Reviews*, *250*, p.104699. https://doi.org/10.1016/j.earscirev.2024.104699

Romans, B. W., Castelltort, S., Covault, J. A., Fildani, A. & Walsh, J. P. (2016) Environmental signal propagation in sedimentary systems across timescales. *Earth Science Reviews*. 153, 7-29. 10.1016/j.earscirev.2015.07.012

Safriel, U, Adeel, Z, Niemeijer, D, Puigdefabregas, J, White, R, Lal, R, Winslow, M, Ziedler, J, Prince, S, Archer, E & King, C 2005, Dryland Systems. in R Hassan, R Scholes & N Ash (eds), Ecosystems and human well-being: current state and trends. Island Press, Washington, pp. 623-662.

Sandercock, P.J., Hooke, J.M. and Mant, J.M., 2007. Vegetation in dryland river channels and its interaction with fluvial processes. *Progress in Physical Geography*, *31*(2), pp.107-129. https://doi.org/10.1177/0309133307076106

Sass, K., von Eynatten, H., Meyerink, T., Schade, J. and Dunkl, I., 2023. Heavy mineral constraints on the evolution and provenance of upper Permian and lower Triassic siliciclastic deposits of the Central European Basin. *Journal of Applied and Regional Geology/Zeitschrift der Deutschen Gesellschaft für Geowissenschaften (ZDGG)*, *174*(3). https://doi.org/10.1127/zdgg/2023/0404

Satoh, Y., Yoshimura, K., Pokhrel, Y. et al. The timing of unprecedented hydrological drought under climate change. Nature Communications 13, 3287 (2022). https://doi.org/10.1038/s41467-022-30729-2

Sharma, N., Whittaker, A.C., Watkins, S.E., Valero, L., Vérité, J., Puigdefabregas, C., Adatte, T., Garcés, M., Guillocheau, F. and Castelltort, S., 2023. Water discharge variations control fluvial stratigraphic architecture in the Middle Eocene Escanilla formation, Spain. Scientific Reports, 13(1), p.6834. https://doi.org/10.1038/s41598-023-33600-6

Schellschmidt, R., Sanner, B., Pester, S. and Schulz, R., 2010, April. Geothermal energy use in Germany. In Proceedings world geothermal congress (Vol. 152, p. 19).

Schmitz, B. and Pujalte, V., 2007. Abrupt increase in seasonal extreme precipitation at the Paleocene-Eocene boundary. *Geology*, *35*(3), pp.215-218. https://doi.org/10.1130/G23261A.1

Selwood, E.B., Edwards, R.A., Simpson, S., Chesher, J.A., Hamblin, R.J.O., Henson, M.R., Riddolls, B.W. and Waters, R.A., 1984. Geology of the country around Newton Abbot. Memoir for 1:50,000 geological sheet 339, New Series.

Sendino, C., Taylor, P.D. and Van Iten, H., 2012. Metaconularia? pyramidata (Bronn, 1837): a scyphozoan from the Ordovician of Normandy, France, recorded for the first time as a reworked fossil in the Triassic of Devon, England. *Geodiversitas*, *34*(2), pp.283-296. http://dx.doi.org/10.5252/g2012n2a3

Smith, S.A., 1990. The sedimentology and accretionary styles of an ancient gravel-bed stream: the Budleigh Salterton Pebble Beds (Lower Triassic), southwest England. *Sedimentary Geology*, *67*(3-4), pp.199-219. https://doi.org/10.1016/0037-0738(90)90035-R

Smith, S.A. and Edwards, R.A., 1991. Regional sedimentological variations in Lower Triassic fluvial conglomerates (Budleigh Salterton Pebble Beds), southwest England: some implications for palaeogeography and basin evolution. *Geological Journal*, *26*(1), pp.65-83. https://doi.org/10.1002/gj.3350260105

Steel, R.J. and Thompson, D.B., 1983. Structures and textures in Triassic braided stream conglomerates ('Bunter'pebble beds) in the Sherwood Sandstone Group, North Staffordshire, England. Sedimentology, 30(3), pp.341-367. https://doi.org/10.1111/j.1365-3091.1983.tb00677.x

Sun, Y., Joachimski, M.M., Wignall, P.B., Yan, C., Chen, Y., Jiang, H., Wang, L. and Lai, X., 2012. Lethally hot temperatures during the Early Triassic greenhouse. *Science*, *338*(6105), pp.366-370. https://www.science.org/doi/10.1126/science.1224126

Sun, Y., Ma, L., Joachimski, M.M., Richoz, S., Zhang, Z., Huang, E., Wang, T., Krystyn, L. and Lai, X., 2026. The Triassic carbon cycle in turmoil: A 50-my journey from extinction to renewal. *Geology*. https://doi.org/10.1130/G54560.1

Svendsen, J.B. and Hartley, N.R., 2001. Comparison between outcrop-spectral gamma ray logging and whole rock geochemistry: implications for quantitative reservoir characterisation in

continental sequences. *Marine and Petroleum Geology*, *18*(6), pp.657-670. https://doi.org/10.1016/S0264-8172(01)00022-8

Tooth, S. and Nanson, G.C., 1999. Anabranching rivers on the Northern Plains of arid central Australia. Geomorphology, 29(3-4), pp.211-233. https://doi.org/10.1016/S0169-555X(99)00021-5

Tooth, S. and Nanson, G.C., 2000. The role of vegetation in the formation of anabranching channels in an ephemeral river, Northern plains, arid central Australia. Hydrological processes, 14(16-17), pp.3099-3117. https://doi.org/10.1002/1099-1085(200011/12)14:16/17%3C3099::AID-HYP136%3E3.0.CO;2-4

Tooth, S. and Nanson, G.C., 2004. Forms and processes of two highly contrasting rivers in arid central Australia, and the implications for channel-pattern discrimination and prediction. Geological Society of America Bulletin, 116(7-8), pp.802-816. https://doi.org/10.1130/B25308.1

Trampush, S.M., Huzurbazar, S. and McElroy, B., 2014. Empirical assessment of theory for bankfull characteristics of alluvial channels. Water Resources Research, 50(12), pp.9211-9220. https://doi.org/10.1002/2014WR015597

Tyrrell, S., Haughton, P.D., Souders, A.K., Daly, J.S. and Shannon, P.M., 2012. Large-scale, linked drainage systems in the NW European Triassic: insights from the Pb isotopic composition of detrital K-feldspar. *Journal of the Geological Society*, *169*(3), pp.279-295. https://doi.org/10.1144/0016-76492011-104

Valenza, J.M., Whittaker, A.C., Ganti, V., Greenberg, E., McLeod, J. and Wild, A.L., 2026. Pre-vegetation fluvial sheet sands explained: Bedform and bar architecture evidence for 1.2 Ga rapidly migrating, meandering, and high-sinuosity wandering rivers. Geology, 54(1), pp.30-34. https://doi.org/10.1130/G52858.1

Van Vuuren, D.P., O'Neill, B.C., Tebaldi, C., Sanderson, B.M., Chini, L.P., Friedlingstein, P., Hasegawa, T., Riahi, K., Govindasamy, B., Bauer, N. and Eyring, V., 2026. The scenario model intercomparison project for CMIP7 (ScenarioMIP-CMIP7). *Geoscientific Model Development*, *19*(7), pp.2627-2656. https://doi.org/10.5194/gmd-19-2627-2026

Wang, H., Liu, J., Klaar, M., Chen, A., Gudmundsson, L. and Holden, J., 2024. Anthropogenic climate change has influenced global river flow seasonality. *Science*, *383*(6686), pp.1009-1014. https://doi.org/10.1126/science.adi9501

Wentworth, C. K. 1922. “A Scale of Grade and Class Terms for Clastic Sediments.” Journal of Geology 30: 377–392

Willard, D.A., Nelissen, M., Sluijs, A., Brinkhuis, H., Reichgelt, T., Robinson, M. and Self-Trail, J.M., 2026. Terrestrial ecosystem response to changing temperature and seasonality in the Paleocene-Eocene Thermal Maximum: Shallow marine records from the Salisbury Embayment, USA. *Paleoceanography and Paleoclimatology*, *41*(3), p.e2025PA005278. https://doi.org/10.1029/2025PA005278

Wills, L. J. (1956). Concealed coalfields: a palaeographical study of the stratigraphy and tectonics of mid-England in relation to coal reserves. London: Blackie.

Wills, L.J., 1970. The Triassic succession in the central Midlands in its regional setting. *Quarterly Journal of the Geological Society*, *126*(1-4), pp.225-283. https://doi.org/10.1144/gsjgs.126.1.0225

Whittaker, A.C., Duller, R.A., Springett, J., Smithells, R.A., Whitchurch, A.L. and Allen, P.A., 2011. Decoding downstream trends in stratigraphic grain size as a function of tectonic subsidence and sediment supply. *Bulletin*, *123*(7-8), pp.1363-1382. https://doi.org/10.1130/B30351.1

Wolman, M. G. 1954. “A Method of Sampling Coarse River-Bed Material.” Eos, Transactions American Geophysical Union 35: 951–956.

Wong, M. and Parker, G., 2006. Reanalysis and correction of bed-load relation of Meyer-Peter and Müller using their own database. Journal of hydraulic engineering, 132(11), pp.1159-1168. https://doi.org/10.1061/(ASCE)0733-9429(2006)132:11(1159)

Wood, J., McLeod, J.S., Lyster, S.J. and Whittaker, A.C., 2023. Rivers of the Variscan Foreland: fluvial morphodynamics in the Pennant Formation of South Wales, UK. *Journal of the Geological Society*, *180*(1), pp.jgs2022-048. https://doi.org/10.1144/jgs2022-048

Wood, J., McLeod, J.S., Lyster, S.J. and Whittaker, A.C., 2025. Reply to comment on ‘Rivers of the Variscan Foreland: fluvial morphodynamics in the Pennant Formation of South Wales,

UK'. *Journal of the Geological Society*, *182*(5), pp.jgs2025-087. https://doi.org/10.1144/jgs2025-087

Wright, V.P., Marriott, S.B. and Vanstone, S.D., 1991. A 'reg'palaeosol from the Lower Triassic of south Devon: stratigraphic and palaeoclimatic implications. *Geological Magazine*, *128*(5), pp.517-523. https://doi.org/10.1017/S0016756800018653

Yan, X., Hampson, G.J. and Whittaker, A.C., 2026. A new source-to-sink synthesis of the Middle Triassic Helsby Sandstone Formation (Sherwood Sandstone Group) river system of the British Isles. Journal of the Geological Society, pp.jgs2025-214. https://doi.org/10.1144/jgs2025-214

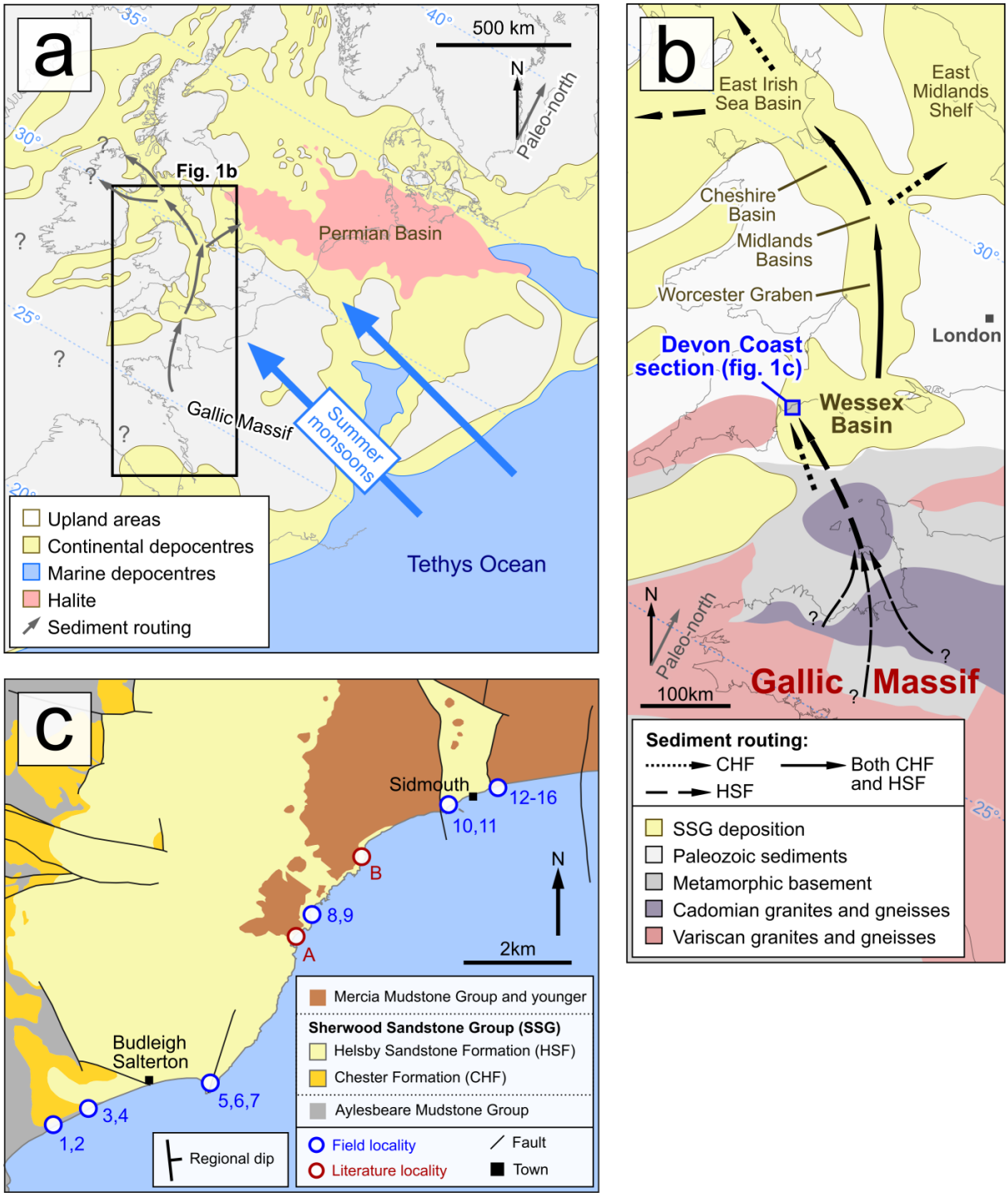


Figure 1: a) Paleogeography of NW Europe during the early to mid-Triassic (adapted from McKie, 2017; Yan et al., 2026). **b)** Source-to-sink sediment routing across north France and the British Isles (Burgess et al., 2025; Yan et al., 2026). **c)** Field localities and distribution of the Sherwood Sandstone Group at outcrop in the Devon study area. Locality A: Lorsong and Atkinson (1994), B: Newell and Shariatipour, 2016. CM: Cornubian Massif, EISB: East Irish Sea Basin, WB: Wessex Basin. **c)** Geological Map Data BGS © UKRI 2025.

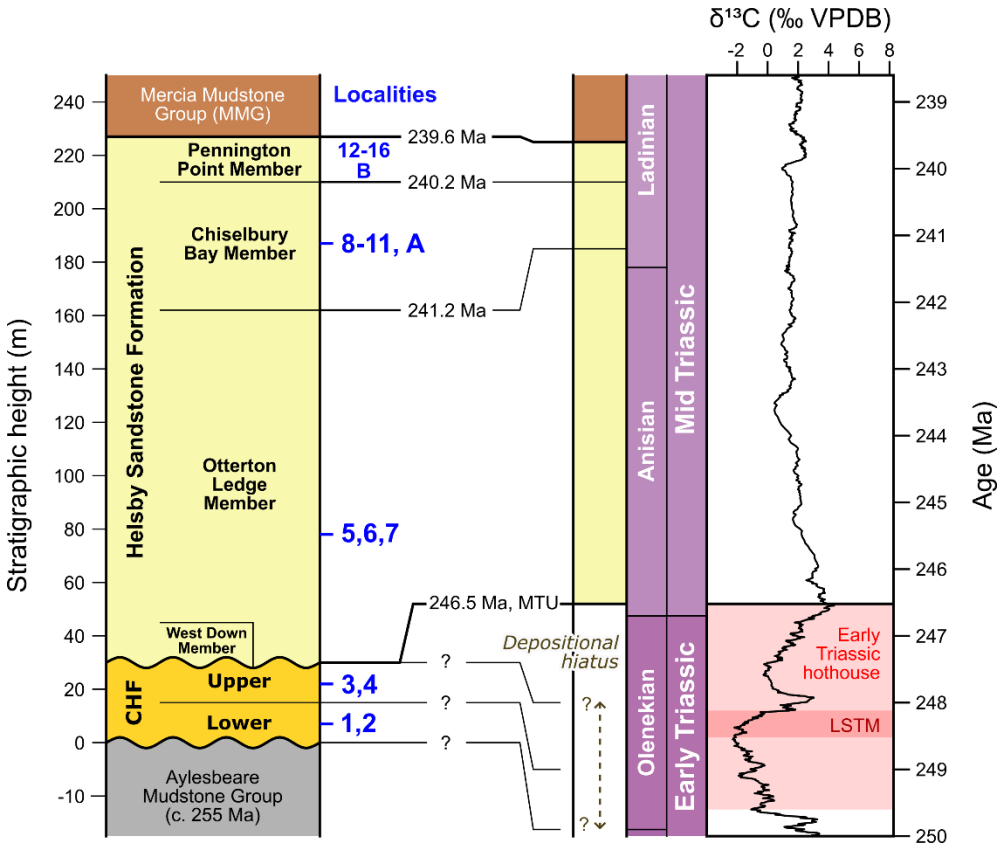


Figure 2: Lithostratigraphy (Smith and Edwards, 1991; Newell, 2017b) and chronostratigraphy (Hounslow and McIntosh, 2003; Hounslow et al., 2017; Hounslow and Gallois, 2023; Yan et al., 2026) for the Devon coastal outcrop section, plotted with the global δ¹³C isotope curve (Ogg et al., 2020; Sun et al., 2026). LSTM: Late Smithian Thermal Maximum, MTU: Mid-Triassic Unconformity, VPDB: Vienna Peedee Belemnite. Localities are the same as in **fig. 1c.**

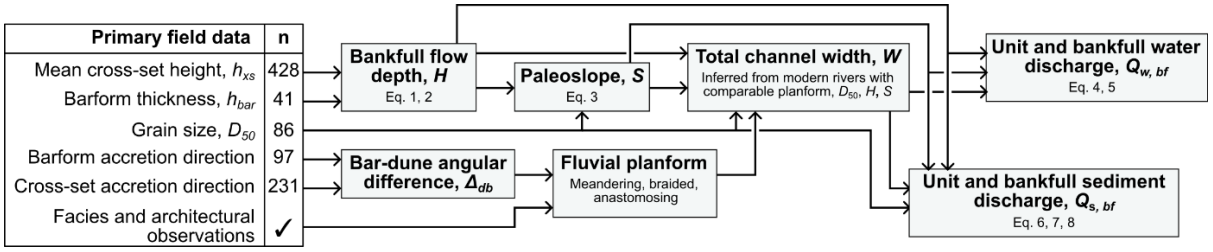


Figure 3: Data analysis flowchart showing the relationship between primary field data and the derivation of key results.

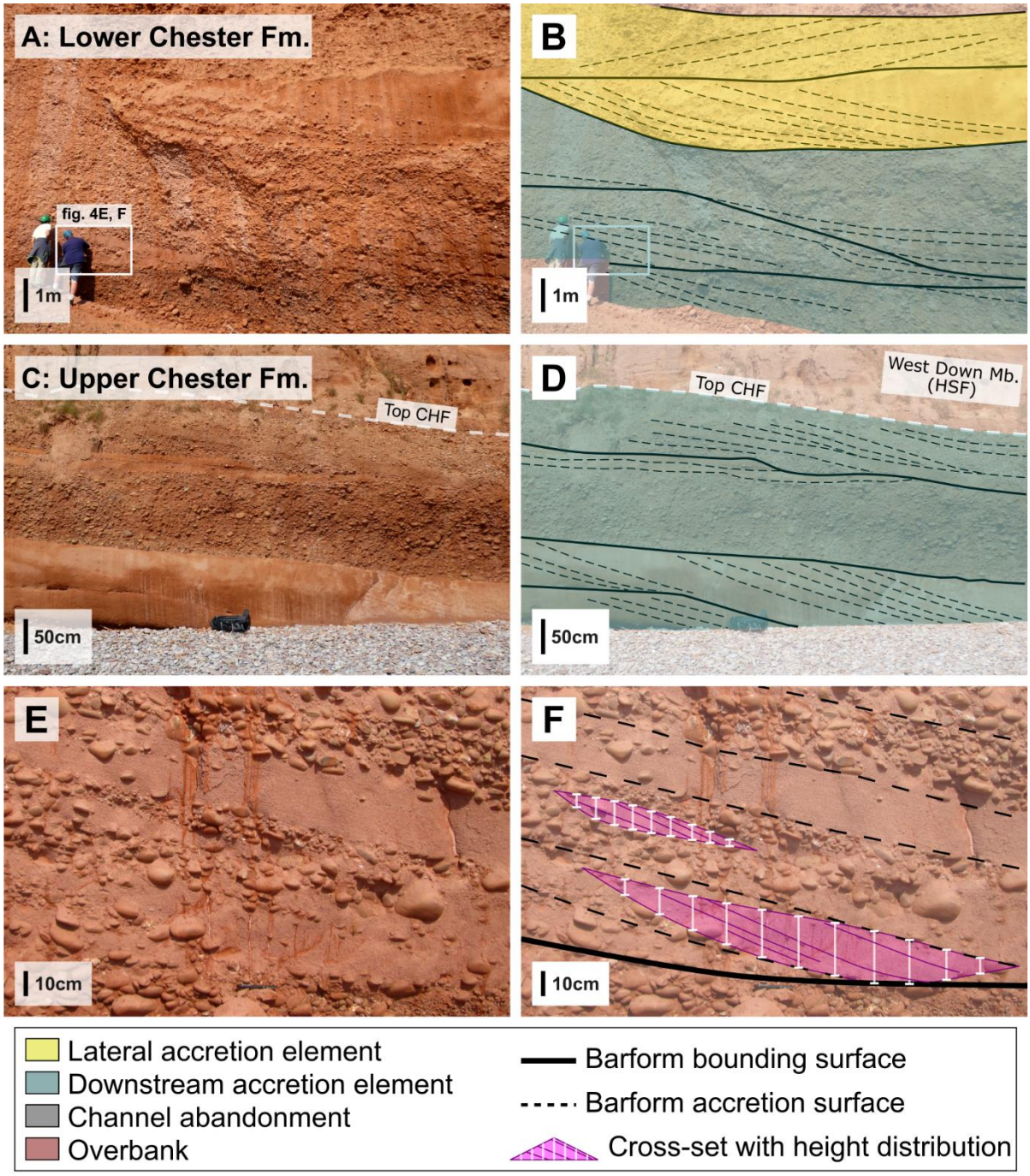


Fig. 4: Representative outcrop photographs of the **a, b)** lower and **c, d)** upper Chester Formation at localities 1 and 4, respectively (**fig. 1c**), with interpreted architectural elements. **e, f)** Cross-sets in the Chester Formation showing measured height distributions. Note the differences in scale between the paired photographs.

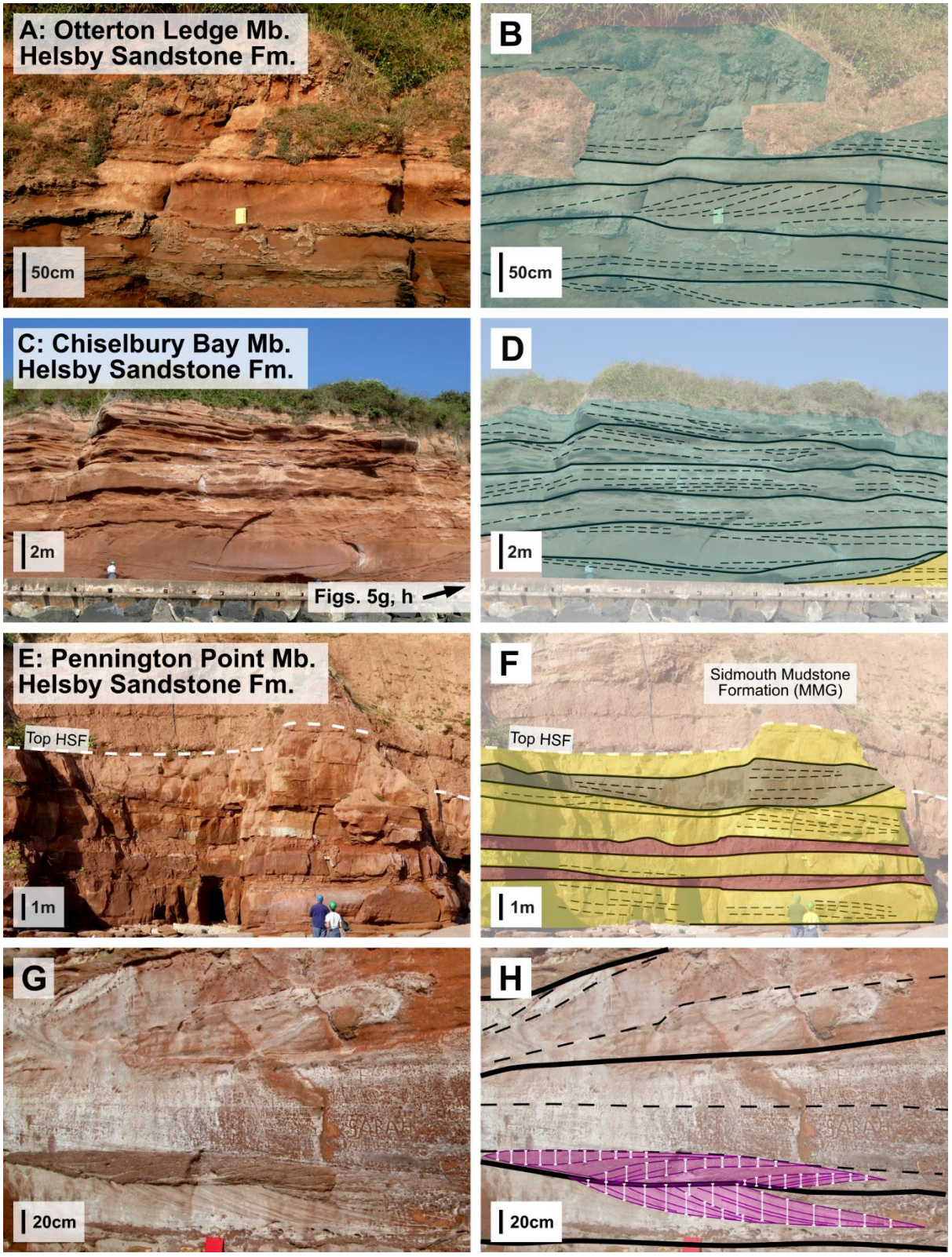


Fig. 5: Representative outcrop photographs of the Helsby Sandstone Formation (HSF) for the **a, b)** Otterton Ledge Member, **c, d)** Chiselbury Bay Member, and **e, f)** Pennington Point Member at localities 6, 10 and 15, respectively (**fig. 1c**), with interpreted architectural elements. **g, h)** Cross-sets in the HSF showing measured height distributions. For clarity, not all cross-sets are annotated. Note the differences in scale between the paired photographs. See **fig. 4** for key.

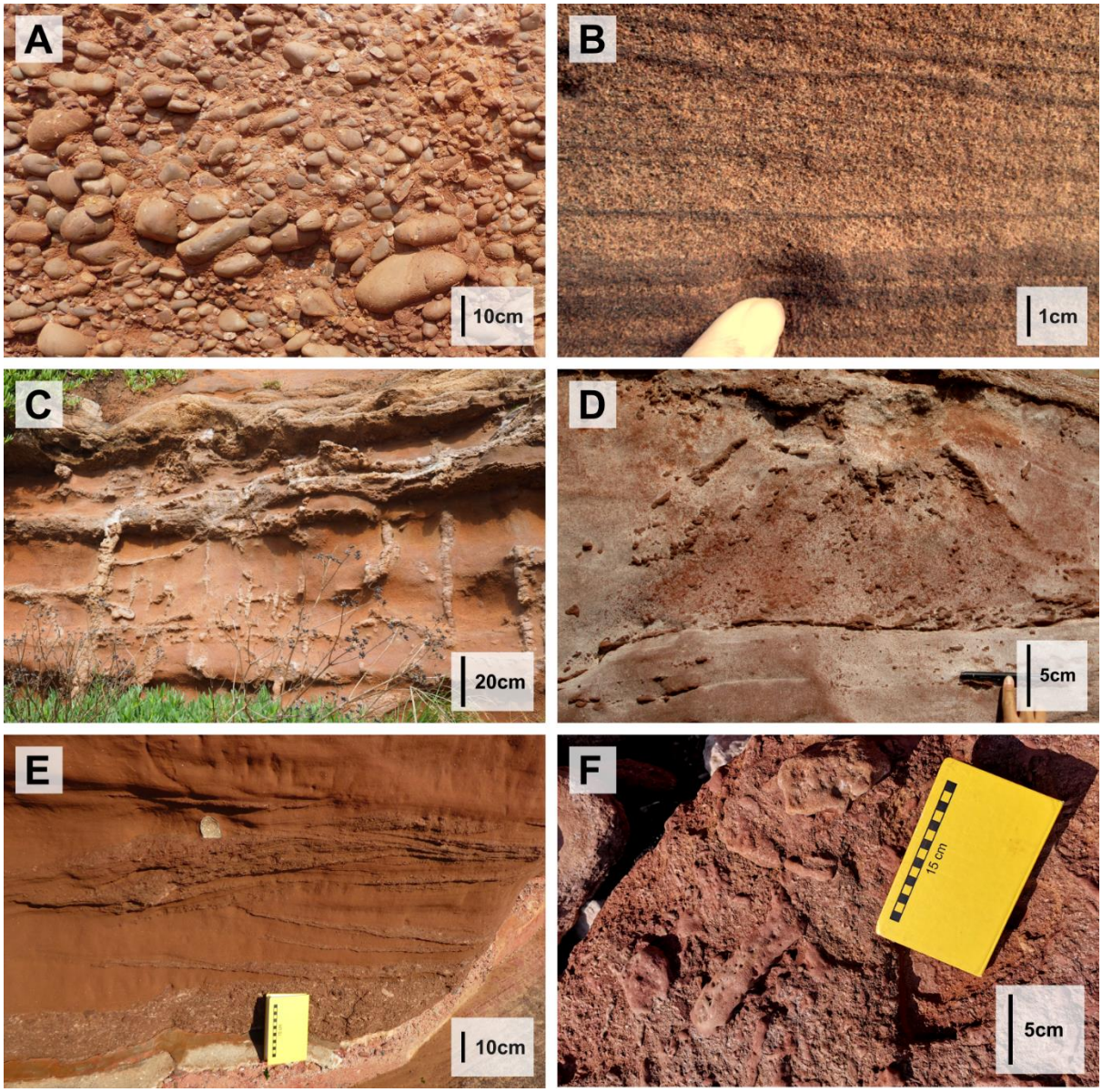
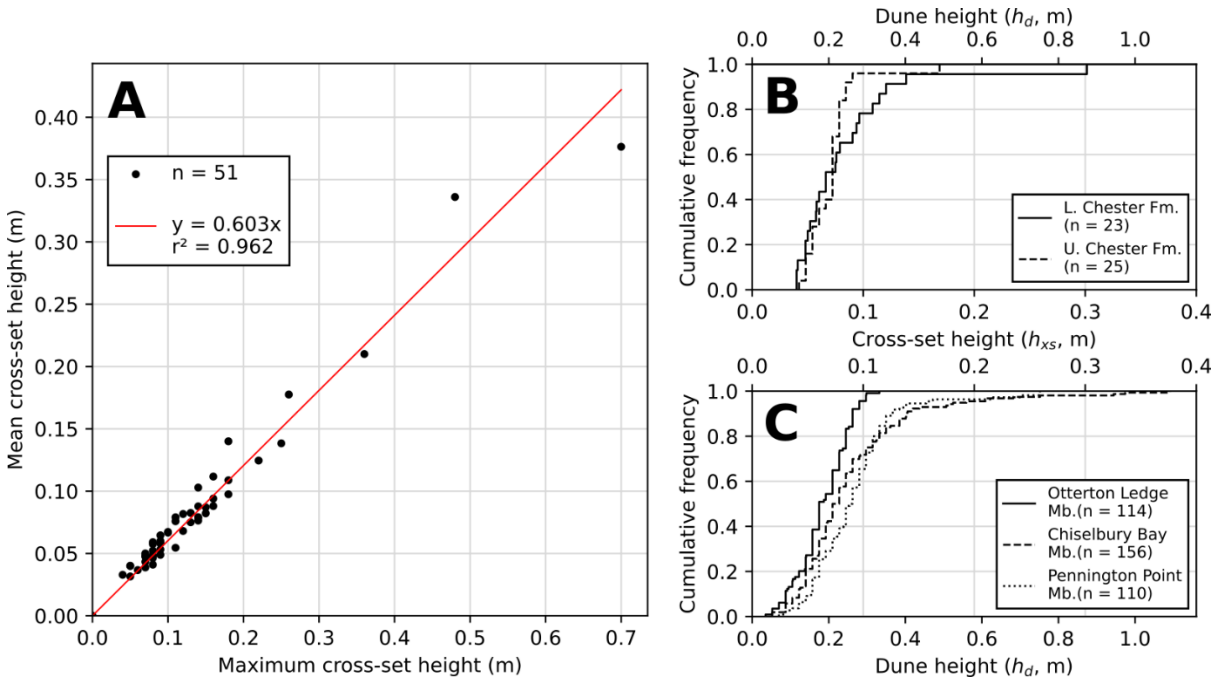


Figure 6: Representative grain size in the **a)** conglomeratic Chester Formation, and **b)** sandstone-dominated Helsby Sandstone Formation (HSF) at localities 1 and 8, respectively (**fig. 1c**). In-situ rhizocretions in the **c)** Otterton Ledge Member, and **d)** Chiselbury Bay Member of the HSF at localities 6 and 11, respectively (**fig. 1c**). Rhizocretions reworked and deposited as gravel lags in the **e)** Chiselbury Bay Member, and **f)** Pennington Point Member of the HSF at localities 11 and 13, respectively (**fig. 1c**).



1370

1371 **Figure 7: (a)** Relationship between mean and maximum cross-set height for measured cross-
1372 sets in the Sherwood Sandstone Group. Trend line is derived from linear regression through
1373 point (0, 0). Cumulative frequency distribution of mean cross-set heights for the (**b**) Chester
1374 Formation, (**c**) Helsby Sandstone Formation.

1375

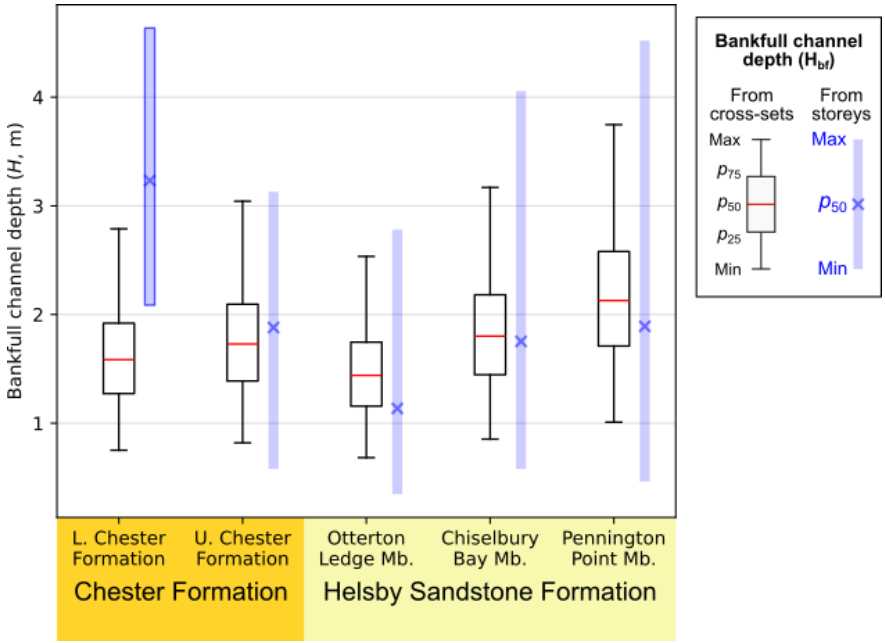
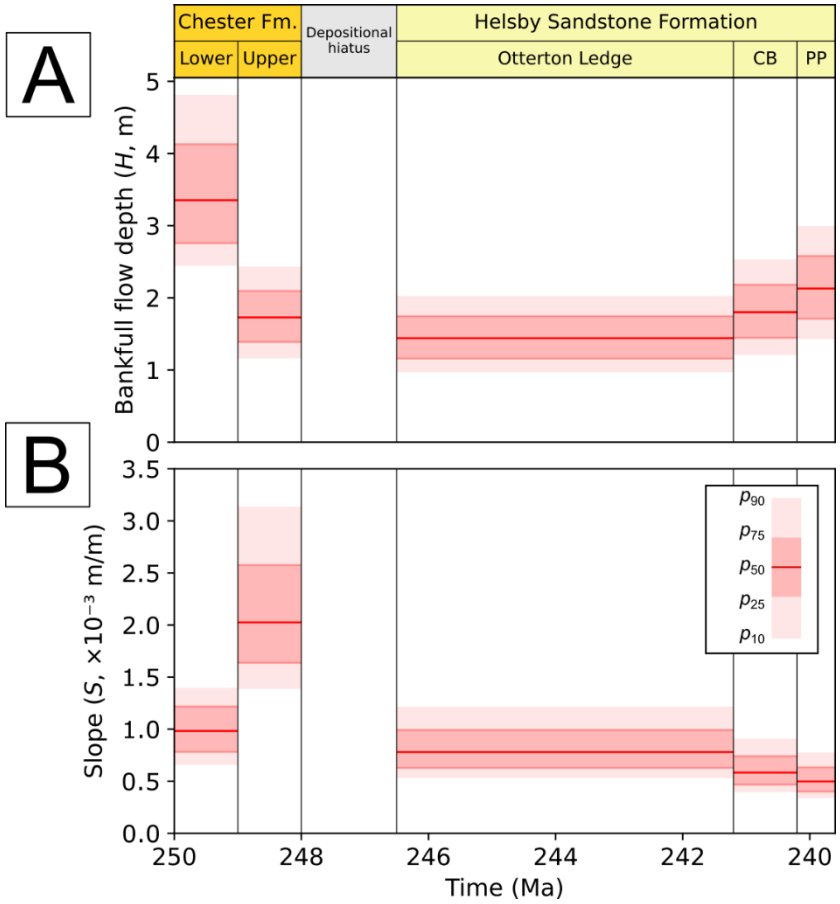


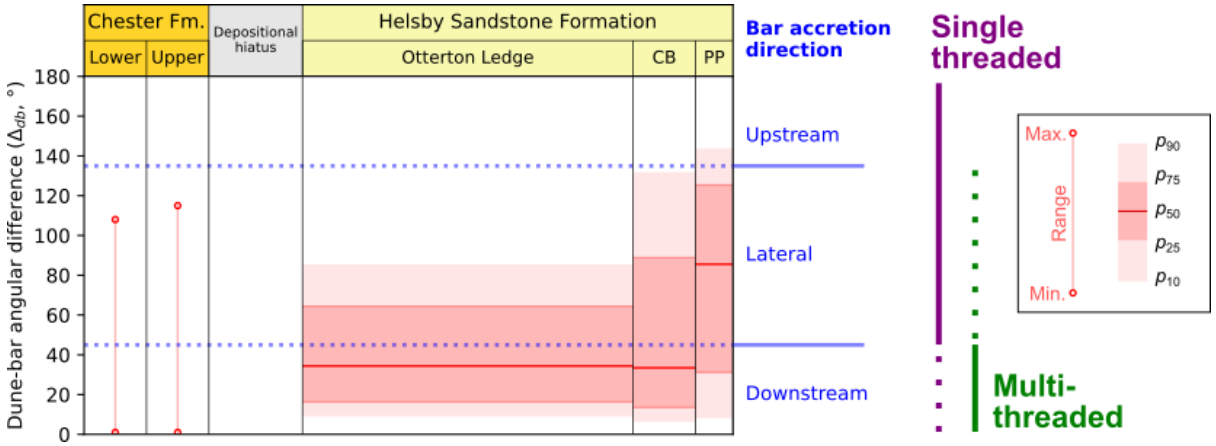
Figure 8: Bankfull flow depth for each lithostratigraphic member of the Chester Formation and Helsby Sandstone Formation, reconstructed by bedform and barform approaches.



1380

1381 **Figure 9:** Temporal evolution of **a**) estimated bankfull flow depth, **b**) estimated slope. CB:
1382 Chiselbury Bay Member, PP: Pennington Point Member.

1383



1384

1385 **Figure 10:** Plot of dune-bar angular difference, a planform-diagnostic parameter, plotted for
1386 the Sherwood Sandstone Group.

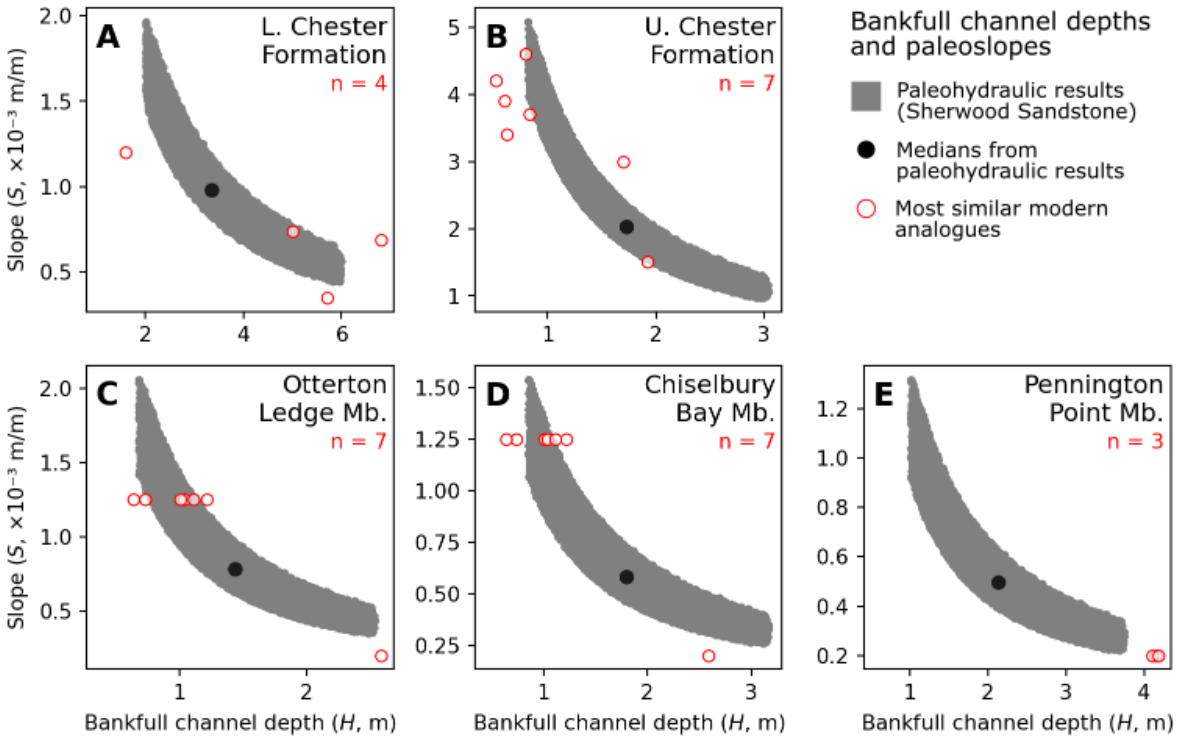


Figure 11 (a-e): Estimated values of slope and channel depth plotted for each stratigraphic division of the SSG (n = 10^5), compared to equivalent parameters in modern rivers of the same bed grain size and planform (Tooth and Nanson, 2004; Brunner, 2013; Nanson and Huang, 2017; Lyster et al., 2022).

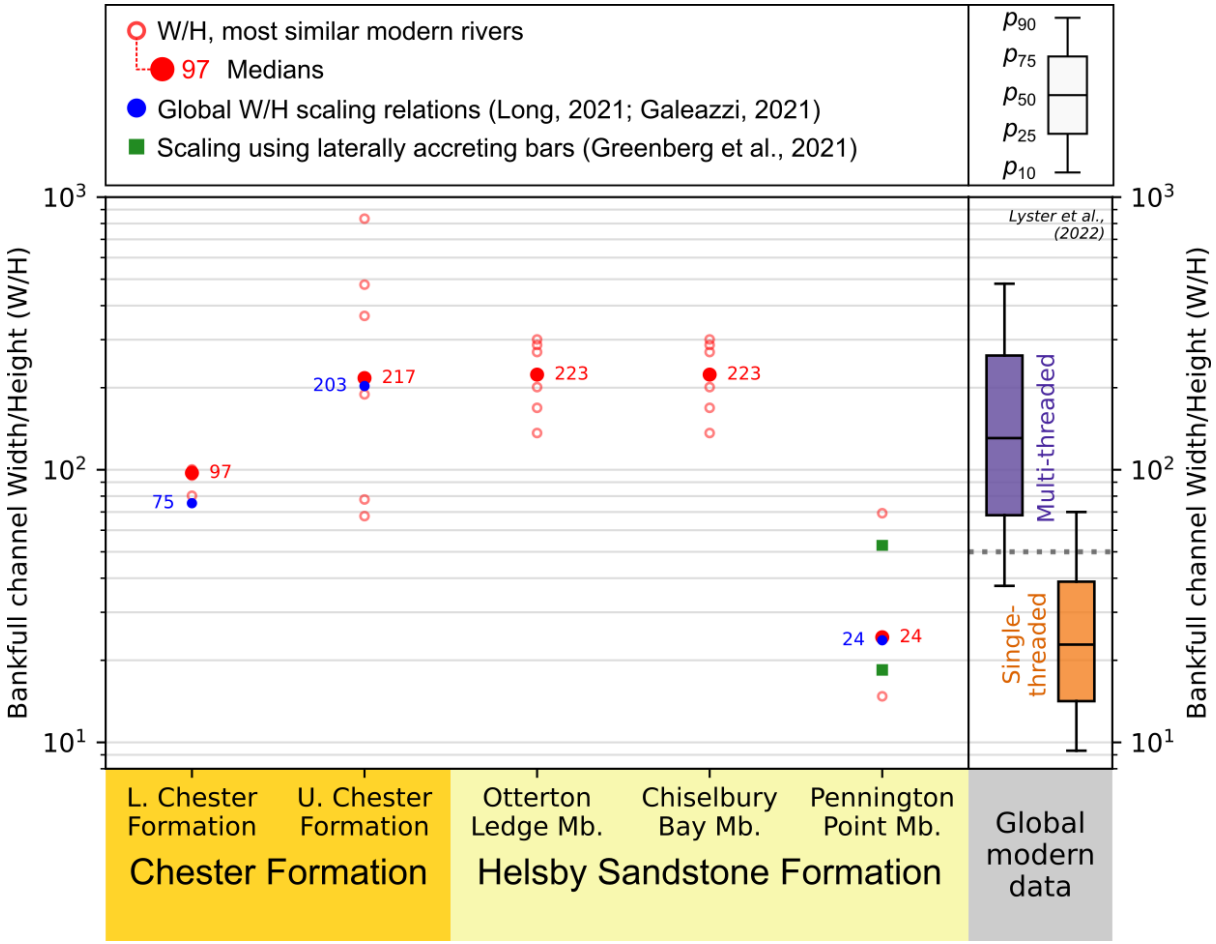


Figure 12: Inferred channel width/depth ratios (W/H) for each division of the Sherwood Sandstone Group, derived using three approaches. W/H is plotted for gemorphically similar modern rivers, which are identified using data in **fig. 11**. Scaling relationships of Long (2021) and Galeazzi (2022) are compiled from global datasets of channel height-width relationships, and channel count, respectively. The scaling relationship of Greenberg et al. (2021) uses laterally accreting bars. These data are compared to a global dataset of modern multi-threaded and single-threaded rivers (Lyster et al., 2022). The grey dashed line correctly classifies 82% of modern single-threaded rivers, and 84% of modern multi-threaded rivers.

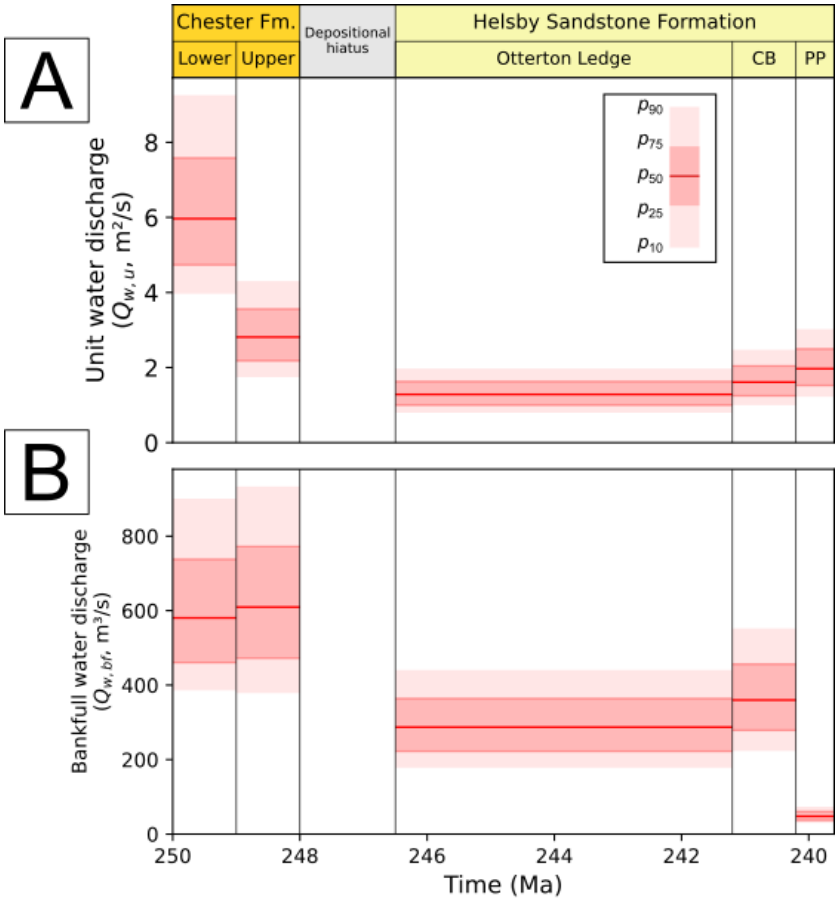
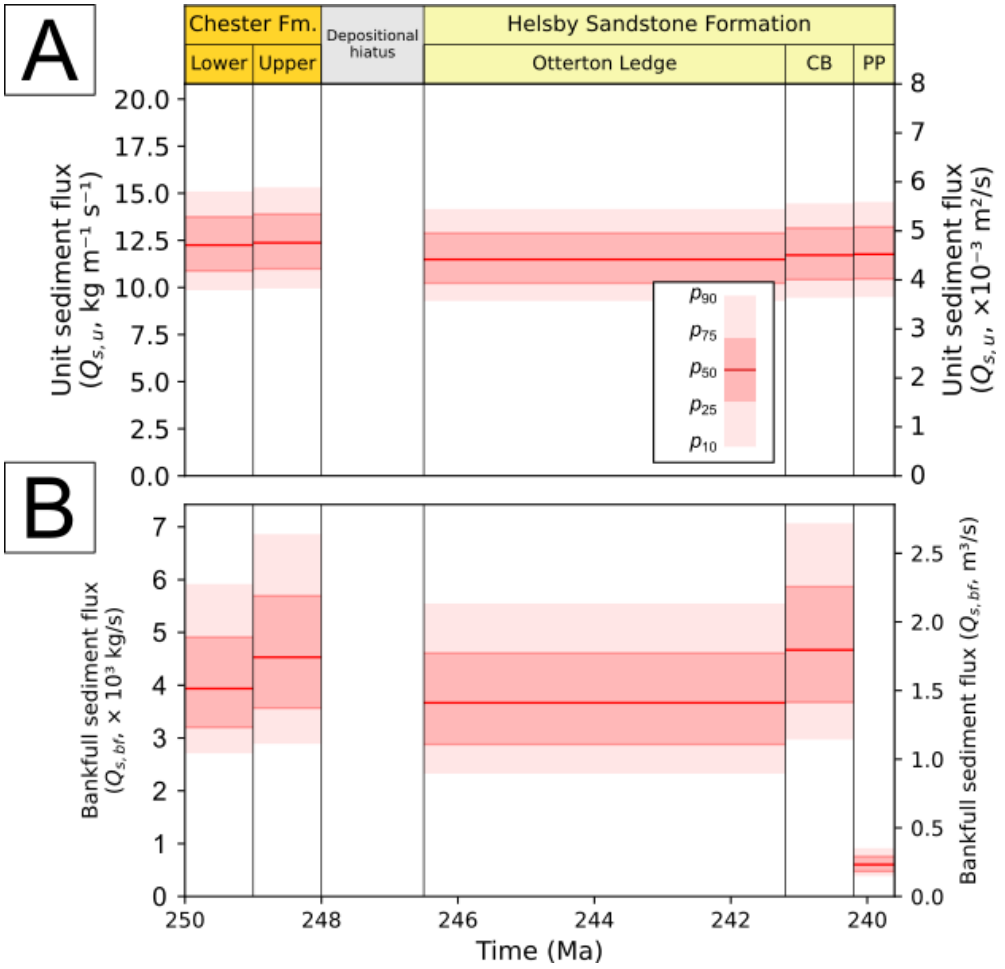


Figure 13: Temporal evolution of **a)** unit and **b)** bankfull water discharge. CB: Chiselbury Bay Member, PP: Pennington Point Member.



1404

1405 **Figure 14:** Temporal evolution of **a)** unit and **b)** bankfull sediment flux. CB: Chiselbury Bay
1406 Member, PP: Pennington Point Member.

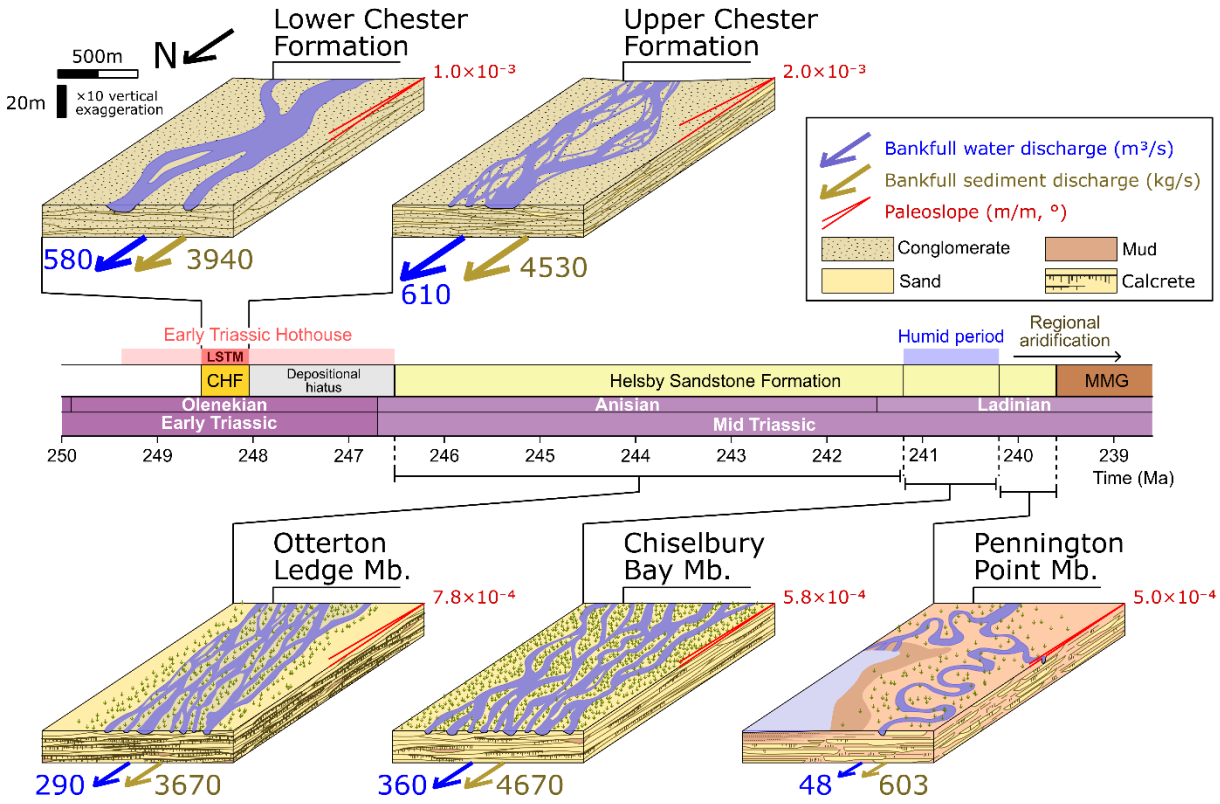


Figure 15: Block diagrams illustrating the temporal evolution of paleoslope, planform, architectural character, bankfull water discharge and bankfull sediment flux in rivers of the SSG in the Devon coastal outcrops. CHF: Chester Formation, LSTM: Late Smithian Thermal Maximum, MMG: Mercia Mudstone Group

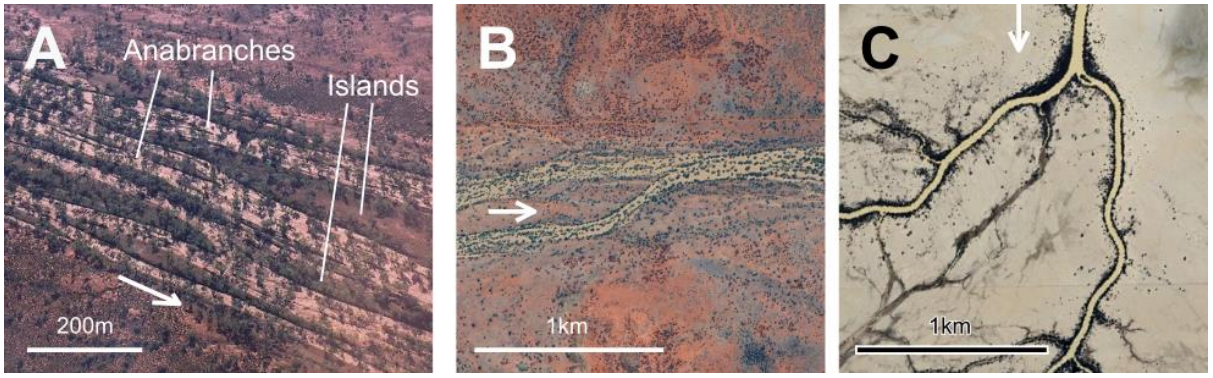


Figure 16: Climatically and geomorphically comparable modern river systems to those interpreted to have deposited the Helsby Sandstone Formation. **(a)** aerial and **(b)** satellite (22.9078° S, 136.0472° E) views of the anastomosing, sand-bed Marshall River, Australia. **c)** satellite view of the sand-bed meandering distributary channels of the Diamantina River, Australia (26.5672° S, 139.2516° E). **a)** from Tooth and Nanson (2000), **b)** and **c)** from Google imagery. White lines indicate flow direction.